Nuclear Engineering and Technology 54 (2022) 3494–3515

Contents lists available at ScienceDirect

Nuclear Engineering and Technology

journal homepage: www.elsevier.com/locate/net

Original Article

Development of nodal diffusion code RAST-V for Vodo–Vodyanoi Energetichesky reactor analysis

Jaerim Jang, Siarhei Dzianisau, Deokjung Lee*

Department of Nuclear Engineering, Ulsan National Institute of Science and Technology, 50 UNIST-gil, Eonyang-eup, Ulju-gun, Ulsan, 44919, South Korea

ARTICLE INFO

Article history:
Received 10 August 2021
Received in revised form
28 March 2022
Accepted 9 April 2022
Available online 14 April 2022

Keywords:
VVER-1000
TPEN
Validation
X2
PWR

ABSTRACT

This paper presents the development of a nodal diffusion code, RAST-V, and its verification and validation for VVER (vodo–vodyanoi energetichesky reactor) analysis. A VVER analytic solver has been implemented in an in-house nodal diffusion code, RAST-K. The new RAST-K version, RAST-V, uses the triangle-based polynomial expansion nodal method. The RAST-K code provides stand-alone and two-step computation modes for steady-state and transient calculations. An in-house lattice code (STREAM) with updated features for VVER analysis is also utilized in the two-step method for cross-section generation. To assess the calculation capability of the formulated analysis module, various verification and validation studies have been performed with Rostov-II, and X2 multicycles, Novovoronezh-4, and the Atomic Energy Research benchmarks. In comparing the multicycle operation, rod worth, and integrated temperature coefficients, RAST-V is found to agree with measurements with high accuracy which RMS differences of each cycle are within ±47 ppm in multicycle operations, and ±81 pcm of the rod worth of the X2 reactor. Transient calculations were also performed considering two different rod ejection scenarios. The accuracy of RAST-V was observed to be comparable to that of conventional nodal diffusion codes (DYN3D, BIPR8, and PARCS).

1. Introduction

This paper presents the verification and validation (V&V) as well as the development of a nodal diffusion code, RAST-V, for VVER (vodo–vodyanoi energetichesky reactor) analysis. The code was developed using an in-house diffusion code, RAST-K, and a triangle-based polynomial expansion nodal method (TPEN) for expanding its area of application [1–3]. The TPEN kernel provides the advantages of pin power reconstruction [3]. The formulated VVER analytic solver was verified using VVER-440 and VVER-1000 benchmarks reported in previous papers [4,5]. A previous study used a macroscopic cross-section but did not include depletion calculation and thermal hydraulic feedback. In contrast, in this work, V&V was performed using various benchmarks with five main calculation features: (1) cross-section feedback (microscopic/macroscopic cross-sections), (2) thermal hydraulic (T/H) feedback, (3) depletion, (4) multicycle calculations (*i.e.*, restart, fuel assembly (FA) shuffling, and rotation), and (5) transient calculation. To assess the calculation capability of these features, V&V was performed with Rostov-II [6], cycles 1–4 of X2 [7–9], Atomic Energy Research (AER) benchmarks (AER-DYN-001 [10] and AER-DYN-002 [11]), and Novovoronezh-4 benchmark [12]. The X2 benchmark problem was used determine the V&V calculation capability in multicycle operation. In contrast, AER-DYN-001 and AER-DYN-002 were used to assess the transient calculation capability, and Novovoronezh-4 was employed to analyze the spent nuclear fuel.

With the increasing share of VVER in the market (currently, US$133 billion), the necessity of VVER analysis has also become increasingly necessary. To date, 71 VVERs are operating and 32 have been contracted [13–15]. Various code systems have been developed for VVER analysis through various projects, including those of PHARE SRR 1/95 [16], VALCO [17], V1000CT [18], Rostov-II [6], Kozloduy [19], Kalinin-3 [20], UAM [21], and AER [22] benchmarks. The Organization for Economic Co-operation and Development/Nuclear Energy Agency and other institutions support these benchmark projects. Moreover, various laboratories have participated in these studies by developing and analyzing their own code systems, such as BKM [23], DYN3D [10], KIKO3D [10], PARCS [24], and TRIKIN [25]. In line with this trend and to improve the competitiveness of nodal diffusion codes formulated in-house, the aforementioned VVER analysis module was developed in RAST-K.

* Corresponding author.
E-mail address: deokjung@unist.ac.kr (D. Lee).

https://doi.org/10.1016/j.net.2022.04.007

Its various features include the following: the use of a micro-depletion solver based on the Chebyshev rational approximation method (CRAM) [1]; provision of various materials for control rod modeling; and additional applications for spent fuel analysis. A spent nuclear fuel (SNF) analysis module is provided for back-end cycle analysis. This study focuses on introducing the formulated calculation features for various V&V benchmark problems, particularly those of Rostov-II, X2 [7–9], AER [10,11], and Novovoronezh-4 [12]. The V&V analysis employs the ENDF/B-VII.0 library [26].

The remainder of this paper is organized as follows. Section 2 describes the calculation modules for VVER analysis, including cross-section feedback and simplified one-dimensional single-channel thermal hydraulic (T/H 1D) feedback scheme. Section 3 presents the reflector model for three-dimensional (3D) core simulation and describes the calculation capability of reflector models. Section 4 presents the depletion calculation results of the X2 reactor. Cycles 1–4 of the X2 reactor were used to assess the calculation capability of RAST-V in multicycle operation. Section 5 presents the transient calculation results of two rod-ejected benchmark problems (AER-DYN-001 and AER-DYN-002). The former is performed with low power; thus, T/H feedback is ignored in this study. In contrast, the latter is implemented with rapid power change; consequently, the Doppler feedback is considered. Section 6 discusses the SNF analysis of sample 21 discharged from Novovoronezh-4.

2. Implementation of hexagonal nodal method in RAST-V

This section presents the calculation features implemented in RAST-V. This code is developed based on RAST-K [1] and TPEN [27], which is capable of pin-power reconstruction. In previous studies, the TPEN kernel was developed and verified through VVER-440 [4] and VVER-1000 [5] benchmarks. In these verifications, the variations of RAST-V are within ±100 pcm, which is comparable to those of other codes. The nodal expansion method (NEM) is employed for analysis in the axial direction, and the coarse mesh finite differential method (CMFD) is adopted for analyzing acceleration. The transient calculation module is developed based on the CMFD with the Wielandt eigenvalue shift method for spatial differential, and the theta method is used for the temporal differential with a theta of 0.5. A second-order precursor integration technique is applied to solve the transient fixed-source problem [28]. The control rod movement and boron dilution are determined in the transient calculation.

Fig. 1 shows the flowchart of RAST-V calculation features: steady-state calculation, transient calculation, and SNF analysis. The steady-state calculation includes eigenvalue and depletion computations. The critical boron concentration (CBC) search option

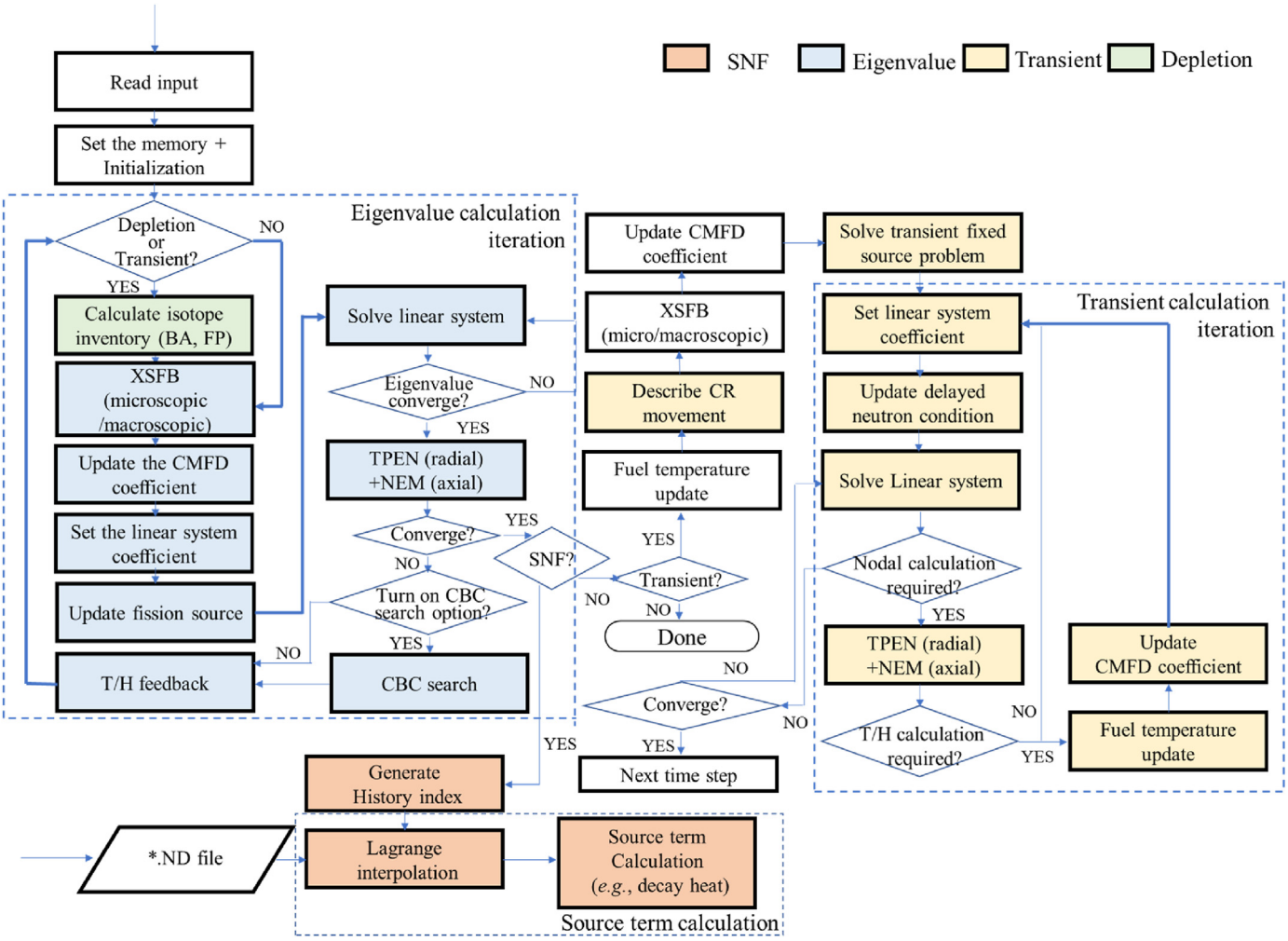

Fig. 1. Flowchart of RAST-V steady state and transient calculation.

is provided for the 3D core simulation. The amounts of burnable absorber (BAs) and fission products are calculated by a micro-depletion calculation module based on CRAM [1]. For computational efficiency, the linear system is set based on the bi-conjugate gradient stabilized (BiCGSTAB) algorithm [29]. The input power condition is used for scaling the flux calculated in the steady state and transient calculations. The T/H 1D feedback is utilized to calculate the Doppler temperature based on inlet temperature and flow rate. An option to use the T/H feedback is available for benchmark analysis, particularly the AER benchmarks described in Section 5. The TPEN kernel defines the flux form as a third-order polynomial and uses the relationship among triangular nodes to identify nine coefficients in the flux form. In the calculation, one hexagonal node is divided into six triangular nodes, as shown in Fig. 2. Subplot (a) presents the six triangular nodes, and subplot (b) contains the flux direction in each node. The centroid of the triangle is the center of mass, and the center in subplot (b) is that of the hexagonal node. Details are presented in Section 2.1. For the application, an SNF analysis module is provided for back-end cycle evaluation. Lagrange interpolation and CRAM are used to calculate the isotope inventory based on the historical indices of main operating parameters; details are described in Section 2.4.

The summary in Table 1 compares the main features of RAST-V with those of other commercial nodal diffusion codes. In particular, the differences are with respect to diffusion equation solver, depletion solver, availability of different materials for control rod modeling, and additional applications (SNF analysis). The calculation feature for the control rod could be used for controlling the VVER-1000 rod composed of B_4C (in the body region) and Dy_2O_3–TiO_2 (in the tip region) [6]. The volume ratio of the control rod material was used for cross-section feedback in the 3D core simulation. In addition, a micro-depletion module based on CRAM was used for calculating the isotope inventory, affording the advantage of large time step depletion with high convergence.

The subsequent section provides details of the foregoing and describes the following calculation modules: analytic solver of hexagonal geometry, cross-section feedback module, T/H feedback solver, and depletion units.

2.1. TPEN method

The TPEN method was implemented in RAST-V based on the references [3,33]. In the TPEN kernel, flux is defined as a third-order polynomial, as shown in Equation (1) [33].

$$\phi_g = c_{1g} + c_{2g}x + c_{3g}y + c_{4g}x^2 + c_{5g}u^2 + c_{6g}p^2 + c_{7g}x^3 + c_{8g}u^3 + c_{9g}p^3, \tag{1}$$

where p and u are the directions combined with x and y, respectively, as shown in Fig. 2. The coefficients, c_{1g}–c_{9g}, are nine unknown values in the homogenized node flux.

Fig. 2 shows six homogenized node fluxes in one hexagonal node, and the six triangular nodes. Because VVER is a light water reactor, the two-group diffusion equation is set as its governing equation for analysis (in contrast, a fast reactor uses 33 groups [34]). The relationships among these six triangular nodes, define the unknown values in Equation (1). Follows nine equations are used to define the nine unknown coefficients: equations of x and y momentums, volume average flux, three of surface average flux equations (x, u, and p direction), and three of corner flux equations (X, U, and P shown in Fig. 2). Equation (2) contains the summary of these nine equations.

where h is the triangle width; ϕ_{gx}, ϕ_{gu}, and ϕ_{gp} are corner fluxes;

$$\begin{bmatrix}
\frac{1}{27} & \frac{1}{27} & \frac{1}{27} & -\frac{12}{27} & -\frac{12}{27} & -\frac{12}{27} & 0 & 0 & \frac{60}{27} \\
\frac{4\sqrt{3}}{9h} & -\frac{\sqrt{3}}{9h} & -\frac{\sqrt{3}}{9h} & 0 & 0 & 0 & \frac{10\sqrt{3}}{h} & 0 & 0 \\
0 & -\frac{2}{3h} & \frac{2}{3h} & 0 & 0 & 0 & 0 & \frac{20}{h} & 0 \\
0 & -\frac{4}{3h^2} & -\frac{4}{3h^2} & \frac{16}{h^2} & 0 & 0 & -\frac{80}{h^2} & 0 & -\frac{40}{3h^2} \\
-\frac{4}{3h^2} & 0 & -\frac{4}{3h^2} & 0 & \frac{16}{h^2} & 0 & \frac{40}{h^2} & \frac{40}{h^2} & -\frac{40}{3h^2} \\
-\frac{4}{3h^2} & -\frac{4}{3h^2} & 0 & 0 & 0 & \frac{16}{h^2} & \frac{40}{h^2} & -\frac{40}{h^2} & -\frac{40}{3h^2} \\
-\frac{16\sqrt{3}}{3h^3} & -\frac{16\sqrt{3}}{9h^3} & -\frac{16\sqrt{3}}{9h^3} & \frac{16\sqrt{3}}{h^3} & \frac{16\sqrt{3}}{3h^3} & \frac{16\sqrt{3}}{3h^3} & -\frac{320\sqrt{3}}{3h^3} & 0 & -\frac{160\sqrt{3}}{3h^3} \\
-\frac{16\sqrt{3}}{9h^3} & -\frac{16\sqrt{3}}{3h^3} & -\frac{16\sqrt{3}}{9h^3} & \frac{16\sqrt{3}}{3h^3} & \frac{16\sqrt{3}}{h^3} & \frac{16\sqrt{3}}{3h^3} & \frac{160\sqrt{3}}{3h^3} & \frac{160\sqrt{3}}{3h^3} & -\frac{160\sqrt{3}}{3h^3} \\
-\frac{16\sqrt{3}}{9h^3} & -\frac{16\sqrt{3}}{9h^3} & -\frac{16\sqrt{3}}{3h^3} & \frac{16\sqrt{3}}{3h^3} & \frac{16\sqrt{3}}{3h^3} & \frac{16\sqrt{3}}{h^3} & \frac{160\sqrt{3}}{3h^3} & \frac{160\sqrt{3}}{3h^3} & -\frac{160\sqrt{3}}{3h^3}
\end{bmatrix}
\begin{bmatrix}
\phi_{gx} \\ \phi_{gu} \\ \phi_{gp} \\ \overline{\phi}_{gx} \\ \overline{\phi}_{gu} \\ \overline{\phi}_{gp} \\ \overline{\overline{\phi}}_{gx} \\ \overline{\overline{\phi}}_{gy} \\ \overline{\phi}_{g}
\end{bmatrix} =
\begin{bmatrix}
c_{1g} \\ c_{2g} \\ c_{3g} \\ c_{4g} \\ c_{5g} \\ c_{6g} \\ c_{7g} \\ c_{8g} \\ c_{9g}
\end{bmatrix}, \tag{2}$$

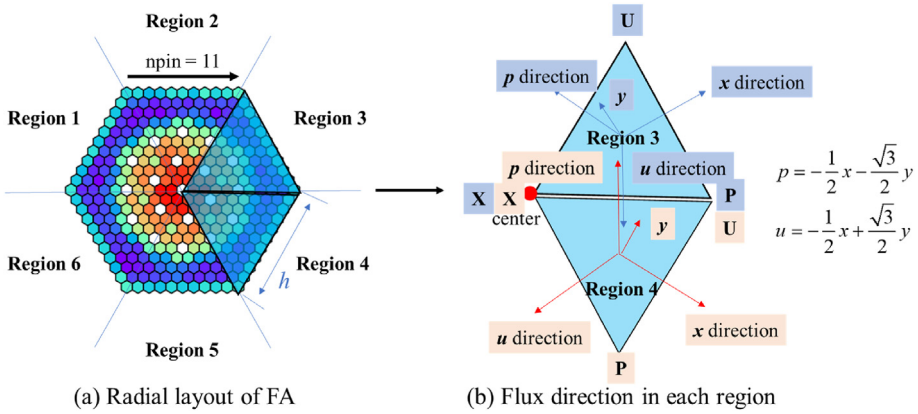

(a) Radial layout of FA (b) Flux direction in each region

Fig. 2. FA and flux direction information.

Table 1
Comparison of nodal diffusion codes.

Parameter	Conventional nodal diffusion codes	RAST-V
Diffusion equation solver	NEM [30]/SANM [31]/AFEN [32]/TPEN [27] - Pros and cons depend on reactor type	TPEN + NEM -Pros: easily splits diffusion equation into group-scale; easily generates pin power reconstruction solution
Depletion solver	Micro-depletion and macro-depletion strategies based on linear interpolation scheme - Pros: fast (saves simulation time) - Cons: limited in providing detail isotope composition for back-end cycle analysis	CRAM-based micro-depletion - Pros: provide isotope inventory information; converges well in long-scale burnup step [2] - Cons: requires long simulation time compared with linear interpolation scheme
Control rod model		Offers various materials for control rod modeling - Pros: considers different control rod materials for tip and body of control rod (*e.g.*, VVER-1000 uses B_4C for control rod body and Dy_2O_3–TiO_2 for tip material)
Additional application		SNF analysis module - Pros: decreases calculation time to reduce SNF analysis step caused by additional code system

$\overline{\phi}_{gx}$, $\overline{\phi}_{gu}$, and $\overline{\phi}_{gp}$ are surface fluxes; $\overline{\overline{\phi}}_{gx}$ and $\overline{\overline{\phi}}_{gy}$ are the x-momentum and y-momentum, respectively; ϕ_g is the average node flux; g is the group number (*e.g.*, 1 or 2).

To get the flux solution, follows equations are solved using equation (1) and matrix equation (2): nodal diffusion balance equation, x-weighted residual equation, y-weighted residual equation, surface average net current, net leakage balance equation at central position of hexagonal geometry [33]. The matrix equation (3) contains a summary of balance equations for the flux solution. Detailed information on matrices is in Ref. [33]. Gaussian elimination is applied to solve the following matrix equation:

$$\begin{bmatrix} A_1 & 0 & 0 & A_2 & A_3 & A_4 \\ 0 & X_1 & 0 & X_2 & X_3 & X_4 \\ 0 & 0 & Y_1 & Y_2 & 0 & 0 \\ S_1 & S_2 & S_3 & S_4 & 0 & 0 \\ Q_1 & Q_2 & 0 & 0 & 0 & 0 \\ 0 & P_1 & 0 & 0 & P_2 & P_3 \end{bmatrix} \begin{bmatrix} \overline{\phi} \\ \overline{\overline{\phi}}_x \\ \overline{\overline{\phi}}_y \\ \overline{\phi}_s \\ \overline{J}_s \\ \phi_c \end{bmatrix} = \begin{bmatrix} \overline{q} \\ \overline{\overline{q}}_x \\ \overline{\overline{q}}_y \\ \overline{q}_s \\ q_j \\ q_c \end{bmatrix}, \tag{3}$$

where the coefficient matrices of A_{1-3}, X_{1-3}, Y_{1-2}, S_{1-4}, and Q_{1-2} are 12×12 matrices: 12 is the number of triangular nodes (6) multiplied by the number of energy group (2); A_4 and X_4 are 12×2 matrices; P_1 and P_2 are 2×12 matrices; and P_3 is a 2×2 matrix. The notations ϕ, J, and q represent the flux, current, and source, respectively. Matrices $\overline{\phi}$, $\overline{\phi}_s$, $\overline{J}_s$, $\overline{\overline{\phi}_x}$, and $\overline{\overline{\phi}_y}$ are the node average flux, surface flux, surface current, x-momentum, and y-momentum, respectively: each matrix is 12×1. The central point flux is ϕ_c with a matrix size of 2×1; 2 is the number of energy group.

Sources used in TPEN, are defined from axial NEM solutions. The detail derivation is presented in the appendix. Table 2 shows the calculation flow of non-linear TPEN solver coupled with linear system. Before update incoming current, boundary conditions are defined based on flux generated by linear system. Radial source, incoming current, and corner fluxes are used for input to solve the radial TPEN. In addition, two node CMFD method is used for accelerations.

Further, flux solution is used in pin power reconstruction. Because the flux form is a polynomial, as shown in Equation (1), the pin flux is facilely calculated using the positions of x and y; p and u are converted using $p = -1/2*x - \sqrt{3}/2*y$ and $u = -1/2*x + \sqrt{3}/2*y$, respectively, as shown in Fig. 2. The TPEN method facilitates group number addition and pin power reconstruction. Because the hexagonal node has six different homogenized fluxes as a triangular node scale, the nine coefficients of each homogenized flux have different values in each triangle node. Six different fluxes were used for pin-power reconstruction with different x and y positions at each pin location. The notation *npin* is the pin number located on one side of the hexagon; Fig. 2 (a) shows the sample hexagon with $npin = 11$. The FA model is obtained from the VVER-1000 model [6]. Pin power reconstruction is implemented based on Equation (4), as follows:

$$P_{pin}(x,y) = P_{homo}(x,y) * P_{FF}(x,y) = \left(\kappa\Sigma_{f1}\phi_1(x,y) + \kappa\Sigma_{f2}\phi_2(x,y)\right) * P_{FF}(x,y), \tag{4}$$

where P_{pin} is pin power; P_{homo} is the calculated pin power through the homogenized node flux (*i.e.*, the power calculated by TPEN flux in Equation (1) using the pin location (x and y positions)); P_{FF} is the

Table 2
Calculation flow of Non-linear TPEN solver.

Order	Content	Input	Output	Method
1	Update Incoming current	Outgoing current	Incoming current	
2	Update corner flux	Average flux, surface flux	Corner flux	Corner flux current balance method [33]
3	Update axial calculation conditions	Incoming current, average flux	Outgoing current, average flux, axial source	1D NEM
4	Update radial source	Axial source	Radial source	
5	Update radial calculation conditions	Incoming current, corner flux, radial source	Average flux, x-direction momentum, y-direction momentum, surface current (u and p direction), outgoing current (x direction), center point flux	TPEN [33]
6	Update D_hat and beta for CMFD	Surface current, surface flux	D_hat and beta	

form function generated by lattice code STREAM; $\kappa\Sigma_{f1}$ and $\kappa\Sigma_{f2}$ represent kappa (energy released per fission) multiplied by fission cross section of groups 1 and 2, respectively. Pin power reconstruction is used to detect the maximum pin power for safety analysis, and to calculate the pin-scale isotope inventory for back-end cycle analysis. Section 4.2 presents the pin power reconstruction module for a small core composed of 37 FAs.

2.2. Cross-section feedback and TH feedback model

This section describes the feedback model used in RAST-K calculation. Sections 2.2.1 and 2.2.2 present the calculation feature of cross-section feedback, and Section 2.2.3 describes the T/H feedback module used in 3D calculation. The linkage code, STORA (STREAM TO RAST-K) [2], is used to reformat the group constants (*i.e.*, cross-section data, assembly discontinuity factor (ADF), and corner discontinuity factor (CDF)) for the two-step calculation method.

2.2.1. Macroscopic cross-section feedback

Macroscopic cross-section feedback is performed based on linear interpolations under five calculation conditions: boron concentration, fuel temperature, moderator temperature, moderator density, and control rod. Table 3 lists the necessary and optional parameters used for core simulation. For the control rod (CR), two types can be considered, that is, two different materials can be maximized for the CR tip and body regions.

In a previous study, to assess the calculation capability of the macroscopic cross section feedback implemented in RAST-V, verification was performed with Kalinin-3 benchmark [5,35]. The NEMTAB format cross-section was used in this comparison, and the ATHLET/KIKO3D [36] code was employed for code-to-code comparison. The results of RAST-V are accurate and comparable to those of ATHLET/KIKO3D, achieving a difference of ±71 pcm [5].

2.2.2. Microscopic cross-section feedback

Microscopic cross-section feedback is performed based on non-linear interpolation. The flowchart of nodal diffusion calculation considering a microscopic cross-section is presented in Fig. 3. A microscopic cross-section is also used for the two-step calculation method. Few-group constants are generated by STREAM. The lattice code STREAM uses the pin-based slowing down method (PSM) for resonance treatment [37]. Predictor-corrector algorithm is used for depletion calculation similar with Serpent 2 [38]. CRAM is adopted to solve the depletion chain with 1640 isotopes. The number densities and microscopic cross sections of 36 isotopes (22 actinides, 12 fission products, and 2 burnable positions [39]) are provided by STREAM for RAST-V micro depletion solver. Depletion calculation capability is presented in section 4.1 by comparing against the Serpent 2 solutions. OpenMP is adopted for acceleration by parallel computations. For the reflector region, 1D and 2D radial reflector

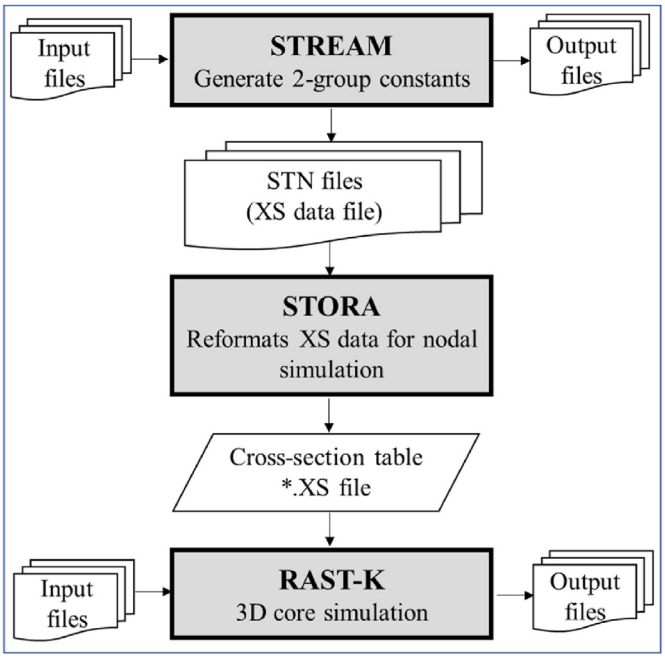

Fig. 3. Flowchart of STREAM/RAST-V two-step method.

Table 3
Macroscopic cross-section feedback parameters.

Case	Necessary parameter	Optional parameter
Base	$\Sigma_{tr,g}$, $\Sigma_{a,g}$, $\Sigma_{n2n,g}$, $\Sigma_{s,g}$, $\Sigma_{f,g}$, $\kappa\Sigma_{f,g}$, $\nu\Sigma_{f,g}$, χ_g	ADF, CDF
Perturbation (Parameters: moderator temperature, fuel temperature, boron concentration)		$d\Sigma_{tr,g,p}$, $d\Sigma_{a,g,p}$, $d\Sigma_{n2n,g,p}$, $d\Sigma_{s,g,p}$, $d\Sigma_{f,g,p}$, $d\kappa\Sigma_{f,g,p}$, $d\nu\Sigma_{f,g,p}$, $d\chi_{g,p}$, $d\mathrm{ADF}_{CR}$, $d\mathrm{CDF}_{CR}$ (g = group, p = parameter, CR = control rod)

model is provided and detail information is presented in section 3.

Data for 3D simulation are reformatted by STORA. A total of 28 branch calculation conditions are used for generating basis cross-section data for the cross section feedback, as listed in Table 5 [2]. The notations *BOR, TFU, TMO,* and *DMO* are reference condition, boron concentration, fuel temperature, moderator temperature, and moderator density, respectively. These branch conditions are defined as combinations of calculation cases. The microscopic cross-section feedback is used to solve the benchmark problems. Table 4 summarizes the list of few-group constants formatted by STORA and employed for microscopic cross-section feedback in the RAST-V calculation. The list includes the ADF, CDF, macroscopic cross-section, microscopic cross-section, delayed neutron, kinetics parameter, decay constants, fission yields, and form functions. The fission yield values are obtained from JANIS-4.0 [41]: ENDF/B-VII.0 [26] and ENDF/B-VII.1 [42] data are provided. In addition, general information is listed in this table for cross-section feedback. For instance, state points are used for nonlinear interpolation.

2.2.3. T/H feedback model

The T/H 1D feedback model was used in the 3D core simulation. During the T/H feedback, the gap conductance, inlet temperature, flow rate, and power condition are used for the calculation. The T/H 1D solver has been verified with various benchmark problems as shown in Ref. [2] and modified for the hexagonal-structured FA calculation. The moderator area and amount are corrected to consider the hexagonal geometry. To assess the calculation capability of the T/H solver adapted in RAST-V, its results are compared with those of Rostov-II measurement. Fig. 4 presents the comparison results of the outlet temperature calculated by the T/H 1D solver based on the inlet temperature and flow rate. The inlet temperature and flow rate as a function of time are obtained from the specifications of Rostov-II benchmark [6]. To obtain the Rostov-II benchmark specification, the calculated Doppler temperature is set as $0.3T_{fc}$ (central fuel temperature) + $0.7T_{fs}$ (surface fuel temperature) [6]. With a deviation of ±2 K, the results of RAST-V are accurate and comparable to those of Rostov-II.

2.3. Depletion scheme

2.3.1. Micro-depletion scheme

The micro-depletion chain is shown in Fig. 5. Through this chain, fission products and heavy nuclides are calculated. To assess the calculation capability of the micro-depletion scheme, the variations in the reactivity of calculated isotopes are compared with those of lattice code STREAM. Verification of micro depletion module implemented in RAST-V, is performed in section 4.1 with STREAM.

Based on the restart files, a multicycle operation is implemented. At each calculation point, the files contain the operating conditions (burnup, day, number density, and boron concentrations) as node-scale (calculation unit of nodal simulation) results. More specifically, 22 actinides, 12 fission products, and 2 burnable poisons (^{152}Gd and ^{160}Gd) are calculated using a micro-depletion chain.

2.4. SNF analysis module

This section discusses the calculation module for SNF that has been developed for analyzing pressurized water reactors (PWRs). Various V&V studies involving 116 measurements have been performed using this module [39,43] for the isotope inventory of samples discharged from Takahama-3, TMI-1, Calvert Cliffs-1, Turkey Point-3, and Obrigheim [43]. It has also been used for the V&V of decay heat of samples discharged from Ringhals-2, Ringhals-3, Turkey Point-3, Point Beach-2, and San Onofre-1 [39]. Previous studies have shown that the calculation results have comparable accuracies. The decay heat variation is within ±4.3% in the FA-wise and pin-wise calculations with different number density file formats. Previous V&V studies have focused on the use of square-type FAs. To expand the application area, the module has been modified for VVER analysis. Verification is performed with Novovoronezh-4 benchmark, and results are presented in Section 6. The SNF analysis module is implemented based on Lagrange interpolation with history indices. Compared with the one-step method, this approach is more advantageous in terms of simulation time, as shown in a previous study [39]. The main calculation conditions are used to generate the history indices of boron concentration, fuel temperature, and moderator temperature. Fig. 6 summarizes the SNF analysis modules, specifically those that have been adapted in STREAM and RAST-V. A flowchart of SNF analysis is presented in Fig. 6. STREAM generates the number density files, and RAST-K uses this file for Lagrange interpolation with history indices to calculate the isotope number density by 3D core simulation conditions. In detail, history branch calculation is used to generate the number density files in STREAM. History branch calculation and branch calculation are similar. However, the former modifies the operating conditions (boron condition, fuel temperature, and moderator temperature) before depletion calculation and then do the depletion calculation under modified conditions, the latter do the calculation with changed condition at specific burnup step. Table 6 lists the history branch calculation conditions [39]: ten conditions are used for calculation.

3. Verification of reflector model for two-step calculation

This section presents the verification of the calculation model, particularly the reflector models, for two-step calculations. As shown in a previous study [44], the reflector model has a considerable effect on the edge FA power and changes the in–out tilt in the core calculation. In addition, because different reflector models have different ADFs and CDFs, they affect the reconstructed pin power. For 3D nodal simulations, 1D and 2D radial reflector models are suggested. Fig. 7 describes the nominal, 1D, and 2D radial reflector models. Subplots (b) and (d) present the 2D and 1D radial reflector models, respectively. Smeared material is used for 1D radial reflector model. As shown in the figure, five different radial reflectors are used in five different regions. A supercell model is used to generate the cross-section of a 2D reflector model, and the vacuum boundary technique is employed for calculation according to a previous study [45]. To assess the calculation capability of a radial reflector in core simulation, verification is performed using the Rostov-II 2D core model; its benchmark is derived from Ref. [6]. Fig. 8 presents the difference in radial power among the various reflector models; Serpent 2 is used to generate the reference. The deviations of 1D and 2D reflectors are within ±3.19% and ±2.76%, as shown in subplots (a) and (b), respectively. Both radial reflector models have reasonable accuracy compared with the results of Serpent 2.

To assess the calculation capability of the reflector model in 3D core simulation, the X2 reactor model is used for comparison. The X2 reactor is built with 1D reflector models radially and axially. The calculation is performed at the beginning of cycle (BOC) under hot zero power (HZP) condition. Fig. 9 shows that the verification of radial and axial and results; their relative variations are ±3.93% and ±5%, respectively. Similarly, Serpent 2 is used to calculate the refence results, as presented in Ref. [7]. Because the 1D radial reflector yields reasonable results, the following section presents the use of the 1D reflector model in the X2 calculation. The X2 reactor specifications are presented in Section 4.3.

Table 4
Parameters reformatted by STORA.

Index	Parameters	
1	Macroscopic cross-section (2 groups)	$\Sigma_{tr,g}$, $\Sigma_{a,g}$, $\Sigma_{n2n,g}$, $\Sigma_{s,g}$, $\Sigma_{f,g}$, $\kappa\Sigma_{f,g}$, $\nu\Sigma_{f,g}$ $(g = 1, 2)$
2	Microscopic cross-section (2 groups)	$\sigma_{tr,g}$, $\sigma_{a,g}$, $\sigma_{n2n,g}$, $\sigma_{s,g}$, $\sigma_{f,g}$, $\kappa\sigma_{f,g}$, $\nu\sigma_{f,g}$ $(g = 1, 2)$
3	General information of STREAM calculation	- State points: boron concentration, moderator temperature, fuel temperature - Steam table option - Pressure - Calculated burnup point - Pin map - Heavy metal mass - Initial isotope inventory of 36 isotopes
4	Form function for pin power reconstruction (1 group)	
5	ADF and CDF	$ADF_{i,g} = \frac{\Phi^s_{i,g}}{\phi_{h,g}}$, $CDF_{i,g} = \frac{\Phi^c_{i,g}}{\phi_{h,g}}$ i = surface index (1–6); g represents group number; $\phi_{h,g}$, $\Phi^s_{i,g}$, and $\Phi^c_{i,g}$ represent node average flux, surface flux, and corner flux, respectively
6	Reflector cross-section correction factor [40]	- Factor is defined as $\frac{ADF_{REF}}{ADF_{FA}}$, where ADF_{REF} and ADF_{FA} are assembly discontinuity factors of reflector and FA, respectively. - Optional
7	Kinetic data and delayed neutron data	Delayed neutron decay constant (6 groups), effective delayed neutron faction (6 groups), neutron velocity (2 groups)
8	Xe and Sm chain data	Fission yield [41] for micro depletion scheme

Table 5
Branch case for cross-section feedback.

Case	Condition	Value			Unit
0	Reference	TMO^a_{REF} CR out	TFU^b_{REF} Detector out	BOR^c_{REF}	
1	BOR	0.1	BOR_{REF}*2	2400	ppm
2	TMO	$TMO_{REF} - 25$	$TMO_{REF} + 25$		K
3	BOR TMO	0.1 $TMO_{REF} - 25$	BOR_{REF}*2 $TMO_{REF} + 25$	2400	ppm K
4	TMO TFU	$TMO_{REF} - 25$ $TMO_{REF} - 25$	 1500		K K
5	TMO CR	$TMO_{REF} - 25$ Inserted	$TMO_{REF} + 25$		K
6	TMO Detector	$TMO_{REF} - 25$ Inserted	$TMO_{REF} + 25$		K

a,b, and c represent reference moderator temperature, fuel temperature, and boron concentration, respectively.

4. Verification and validation of steady state hexagonal nodal solver

This section presents the V&V of steady-state calculations in FA-scale and core-scale problems, where the X2 reactor multicycle model and small core model are used. Steady-state verification involves the calculation of isotope reactivity, depletion, rod worth (containing the SCRAM worth), and integrated temperature coefficient. Section 4.1 presents the FA-wise verification calculations of the depletion solver for comparison with the isotope reactivity, and Section 4.2 covers the pin power reconstruction with the small core model (with 37 FAs). Section 4.3 describes the multicycle depletion calculation results from cycles 1–4 of X2, and Sections 4.4, 4.5, and 4.6 elaborate on the V&V of CR worth, SCRAM worth, and integrated temperature coefficient, respectively. In addition, the calculations described in this section are performed based on ENDF/B-VII.0 [26].

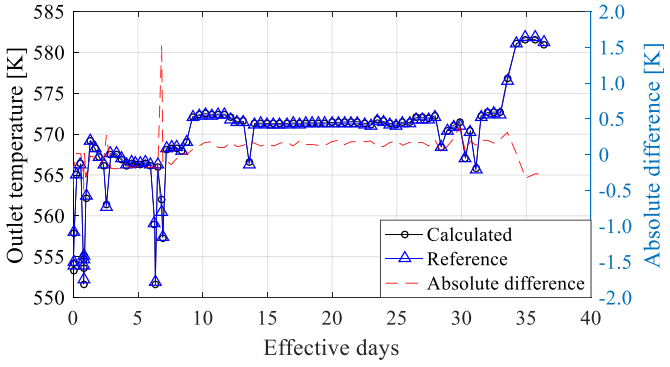

Fig. 4. Outlet temperature calculated by RAST-K VVER.

4.1. Verification of depletion scheme implemented in RAST-V

The micro-depletion chain is shown in Fig. 5. Fission products and heavy nuclides are calculated through this chain. To assess the calculation capability of this scheme, variations in the reactivity of calculated isotopes are compared with STREAM. Fig. 10 presents the depletion results compared with those of Serpent 2, and Fig. 11 shows the detailed reactivity differences among isotopes. The calculations for Serpent 2 are performed with a neutron history of 48 million (*i.e.*, 100 active cycles and 20 inactive cycles each using 400 000 neutrons). The isotope reactivity and reactivity difference are calculated as follows Equation (5) and Equation (6):

$$\Delta\rho = \Sigma_a \Big/ \nu\Sigma_f, \tag{5}$$

$$\Delta\rho_{diff} = \Delta\rho_{ST} - \Delta\rho_{ST/RV} = \left(\Sigma_a \Big/ \nu\Sigma_f\right)_{ST} - \left(\Sigma_a \Big/ \nu\Sigma_f\right)_{ST/RV}, \tag{6}$$

where $\Delta\rho$ is isotope-wise reactivity, and $\Delta\rho_{ST}$ and $\Delta\rho_{ST/RV}$ are isotope-wise reactivity calculated by STREAM and STREAM/RAST-V, respectively. The notation of Σ_a and $\nu\Sigma_f$ are absorption and nu-fission cross section.

The calculated FA model, U22, is referred to Rostov-II as benchmark [6]; it is composed of 2.2 wt% UO_2 fuel. Plutonium and xenon isotopes considerably differ compared with other isotopes; as shown in Fig. 11, all isotopes vary within ±30 pcm. The accuracy of the implemented FA model is comparable to that of lattice code STREAM.

4.2. Verification of pin power reconstruction with small core model

This section presents the verification results of pin power reconstruction with a small-core model, as shown in Fig. 12. The

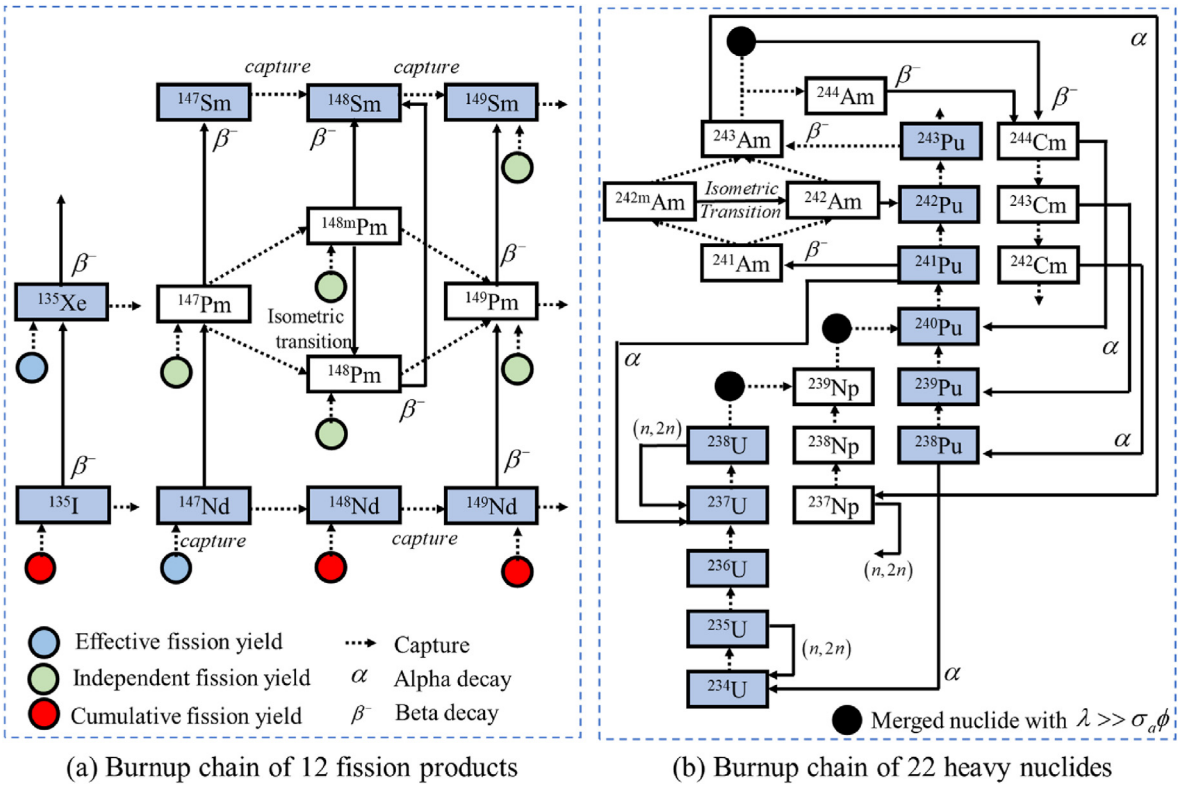

Fig. 5. Depletion chain in RAST-V.

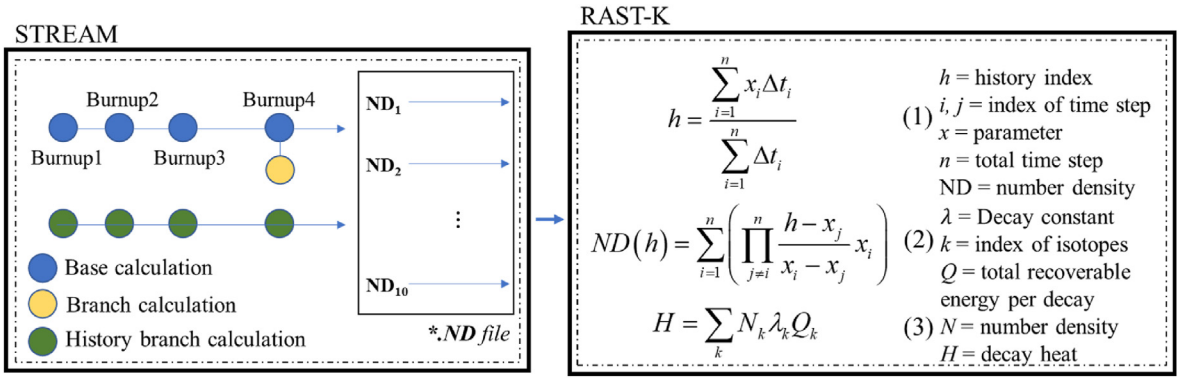

Fig. 6. Flowchart of SNF analysis module.

Table 6
History branch calculation conditions.

Condition	Value	Unit
Reference	TMO_{REF} TFU_{REF} BOR_{REF} (1[a])	
TMO	TMO_{REF} − 40 (2) TMO_{REF} − 20 (3) TMO_{REF} + 20 (4) TMO_{REF} + 40 (5)	K
TFU	TMO_{REF} (6) 1500 (7)	K
BOR	0.1 (8) 2*BOR_{REF} (9) 2400 (10)	ppm

[a] Is order of history branch conditions; 10 conditions are used for calculation.

radial layout of the model is presented in subplot (a), and the reference result is produced by lattice code STREAM. The small core model is composed of U13 and U22 FA models, which are reported in Ref. [6]. To maintain the calculation consistency, ^{238}U resonance up-scattering correction does not consider in STREAM and STREAM/RAST-V calculations. Thermal expansion was not considered in this calculation.

Overall, 11 544 reconstructed pin power values are compared (312 pins in FA and 37 FAs in the core model). Subplot (b) presents pin power distribution calculated by STREAM, and subplot (c) shows the relative difference of STREAM/RAST-V two-step method. Reference value is STREAM and pin power differences are within

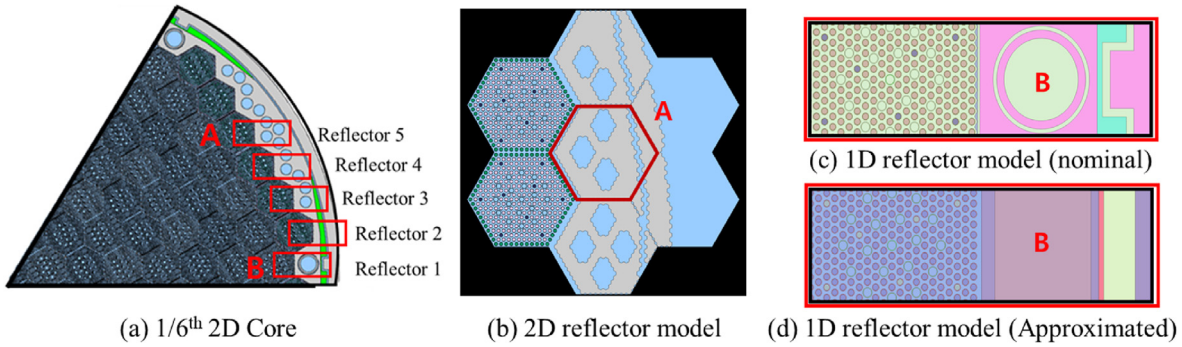

Fig. 7. Reflector model of Rostov-II.

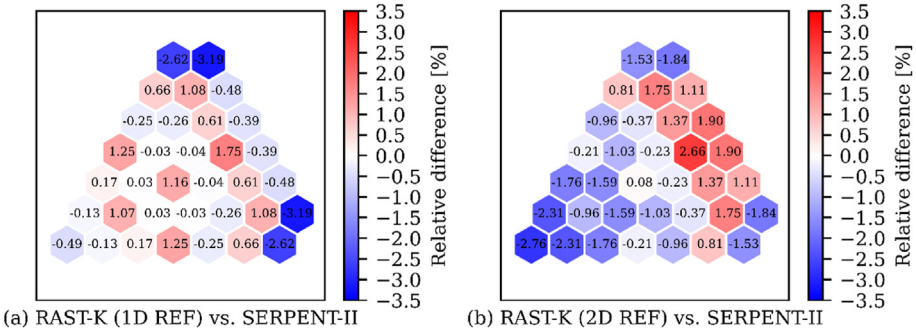

Fig. 8. Radial power difference among various radial reflector models.

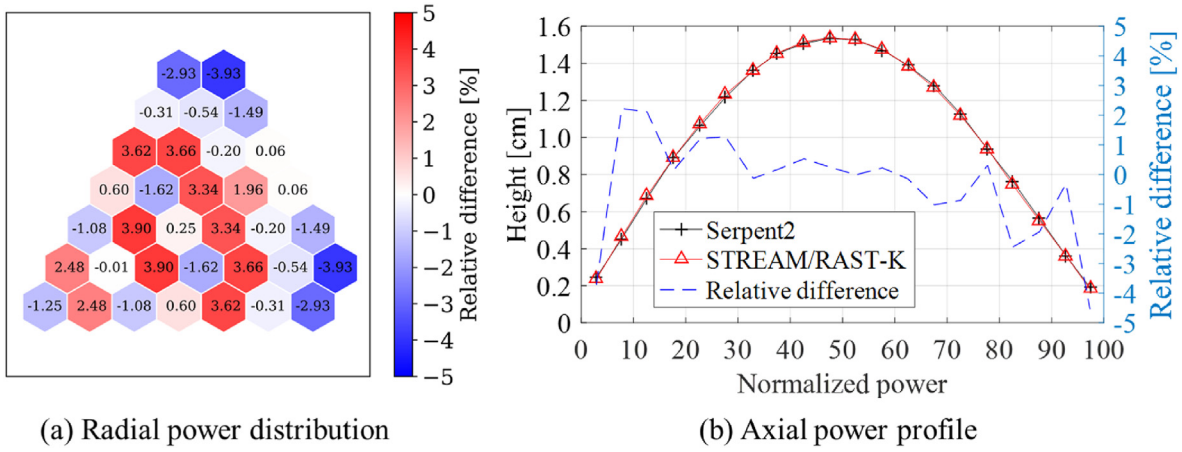

Fig. 9. Radial and axial power profiles.

±3.230%, with the maximum and minimum deviations reaching 2.687% and −3.151%, respectively; the root mean square (RMS) value is 1.061%. The maximum and minimum values are observed near the edge of outer layer FAs. The results are accurate and comparable to those of a previous pin power reconstruction study [46].

4.3. Multicycle depletion

This section presents the multicycle calculation results for assessing the calculation capability of RAST-V. Table 7 summarizes the X2 reactor specifications [7], and Table 8 lists the calculation conditions based on Refs. [8,9]. Detailed T/H conditions, CR positions, and power conditions as functions of time are found in Ref. [8]. In the generation of cross-section data, the pin-based slowing down method [47] is employed for resonance treatment. The up-scattering of ^{238}U is considered in the calculation but thermal expansion is ignored; moreover, inflow transport approximation [47] is applied. As presented in Ref. [7], the top plenum and bottom plenum regions are found in the axial reflectors. The ENDF/B-VII.0 library is employed for calculations [26]. The X2 reactor specifications are summarized in Table 7, and Fig. 13 presents the core loading patterns of X2 multicycles from cycle 1 to cycle 4; the shuffling patterns are shown in Fig. 14. Cycles 1–4 are composed of fresh and burned FAs. The red and blue assemblies are burned FAs; FAs located in the red and blue color positions are from the $(N-1)^{th}$ cycle and $(N-2)^{th}$ cycle, respectively. The index, N, is the number of current cycles. Cycles 2 and 3 utilize the restart file from the

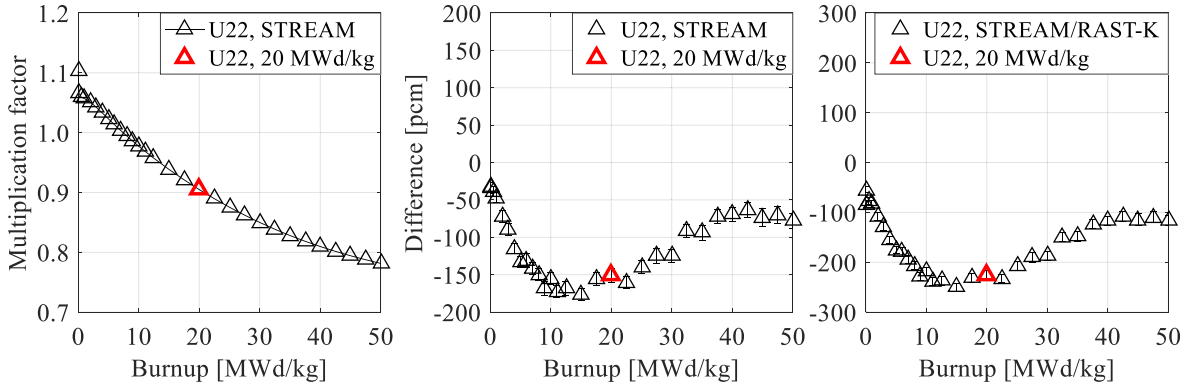

Fig. 10. Depletion of U22 as burnup function.

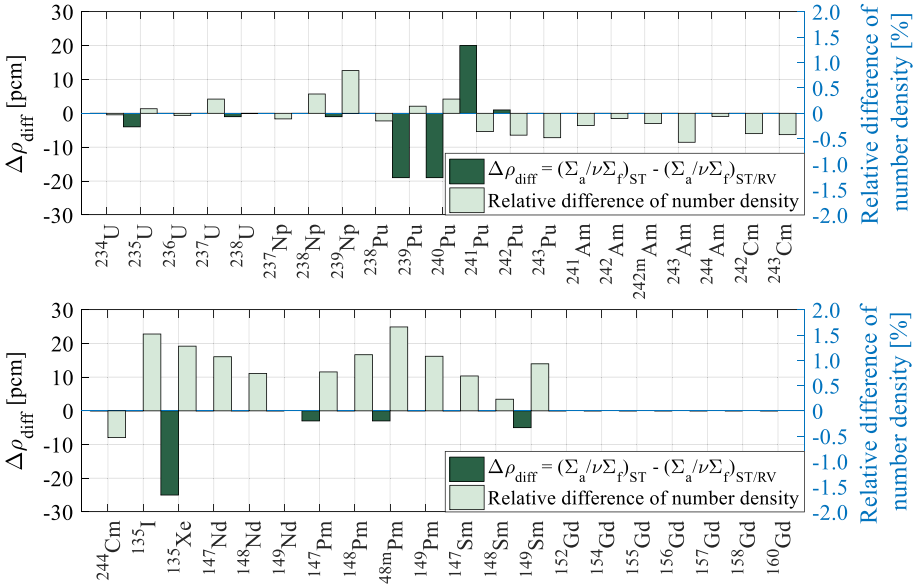

Fig. 11. Comparison of isotope composition in U22 FA.

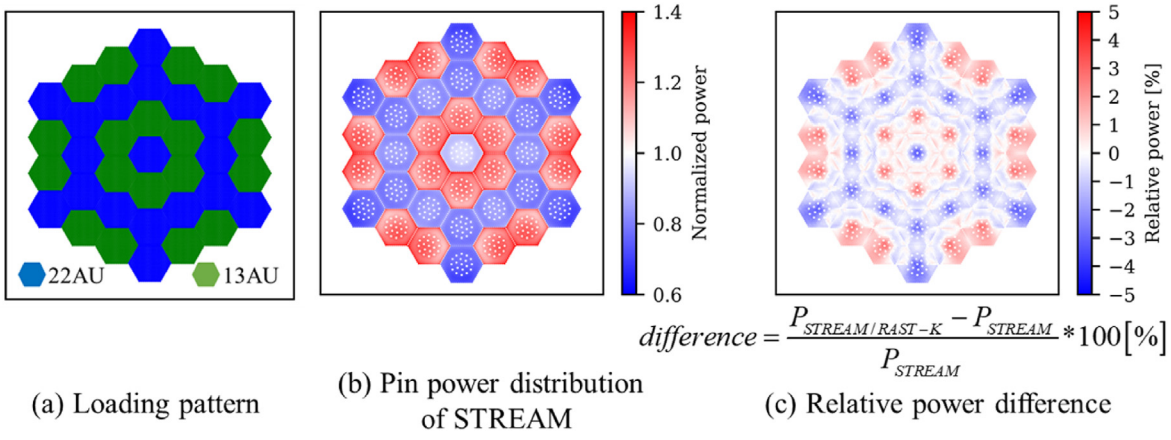

Fig. 12. Pin power difference in small sample core.

previous cycle, and cycle 4 uses multi-restart files from cycles 2 and 3. Therefore, the calculation capability of multicycle depletion, FA shuffling, and FA rotation can be verified through multicycle operation. Table 9 lists the details FAs loaded in the X2 reactor. A total of 163 FAs is loaded into the core. The axial and radial reflector models presented in Section 3 are used for calculation. As shown in the previous section, the power variations of these reflector models

Table 7
X2 reactor specifications.

Parameter	Value	Unit	Parameter	Value	Unit
Active height	353	cm	Number of pins	312	
Number of FAs	163		Number of guide tubes	18	
FA pitch	23.6	cm	Number of instrument tubes	1	
Pin pitch	1.275	cm	FA type	TVSA	
UO_2 density	10.2605	g/cm^3	Spacer grid mass	0.55	kg
Gadolinia density	10.2779	g/cm^3			

Table 8
3D simulation calculation conditions.

Parameter	Value	Parameter	Value
Method of Characteristics ray	0.05 cm	Axial calculation nodes	24 (4 axial reflectors and 20 fuel regions)
Azimuthal angle	96	Reflector height	30 cm (each at bottom and top)
Angle	6	Each calculation node height	17.75 cm
Depletion range (MW•d/kg)	0–50	FA pitch	23.6 cm (face-to-face width)

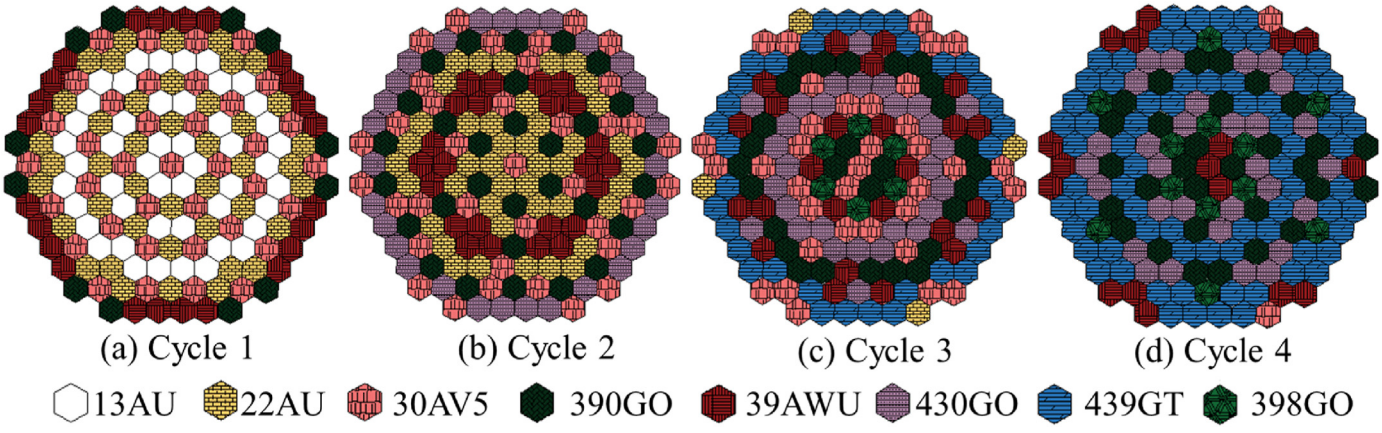

Fig. 13. Core loading pattern of X2 multicycle.

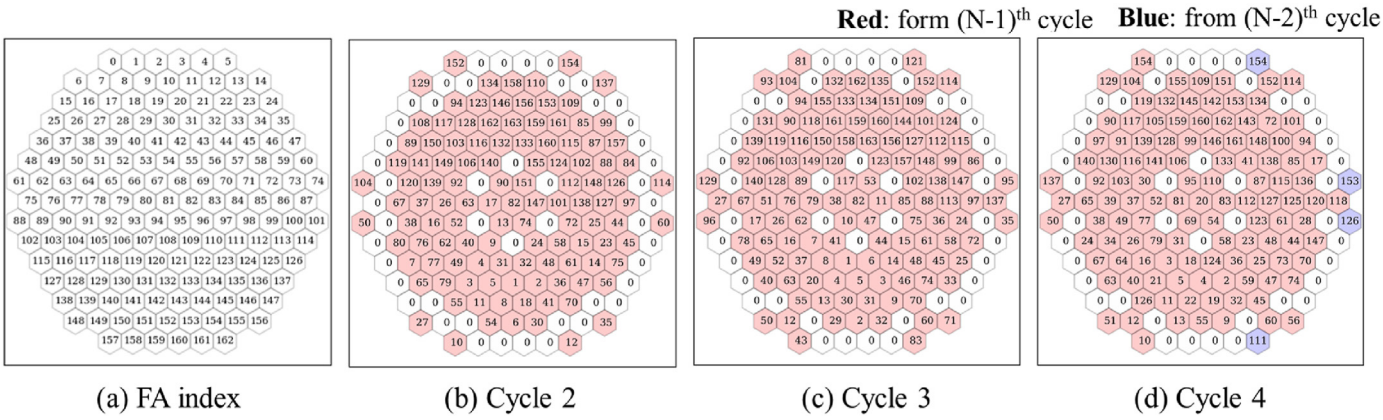

Fig. 14. Shuffling pattern of X2 multicycle.

compared with those of Serpent 2 are within ±5%.

Fig. 15 presents the CBC curves for cycles 1–4. In the computation, 1276 calculation time steps are used, specifically 323, 321, 334, and 298 for calculation in cycles 1, 2, 3, and 4, respectively. Most of calculation results has within ±50 ppm difference boundary compared with measurement. To consult the previous studies, the STREAM/RAST-V has the similar CBC trend compared with other two-step code system calculations (e.g., BIPR-8 [50] and CASMO-5/SIMULATE [49]). As shown in Fig. 15, the variations in cycle 4 exceed those in cycles 1 and 2. Although RAST-V has larger differences in cycle 4, the calculation results are accurate, reaching 0.27 g/kg RMS difference (=47 ppm; 174.88 ppm is 1 g/kg [7]); the results of other nodal diffusion codes exceed 0.63 g/kg. In addition, Table 10 summarizes the multicycle calculation results compared with those of

Table 9
FA specifications in X2 reactor.

FA type	Number of fuel pins/enrichment	Number of gadolinia pins (wt% Gd_2O_3/^{235}U)	Number of FA in core			
			Cycle 1	Cycle 2	Cycle 3	Cycle 4
13AU	312/1.3	–	48	–	–	–
22AU	312/2.2	–	42	42	4	
30AV5	303/3.0	9 (5.0/2.4)	37	37	35	2
39AWU	243/4.0, 60/3.6	9 (5.0/3.3)	24	24	24	17
390GO	240/4.0, 66/3.6	6 (5.0/3.3)	12	30	28	30
398GO	306/4.4	6 (5.0/3.3)	–	–	6	12
430GO	240/4.4, 66/4.0	6 (5.0/3.6)	–	30	30	30
439 GT	306/4.4	6 (5.0/3.6)	–	–	36	72
Total number of FAs			163	163	163	163

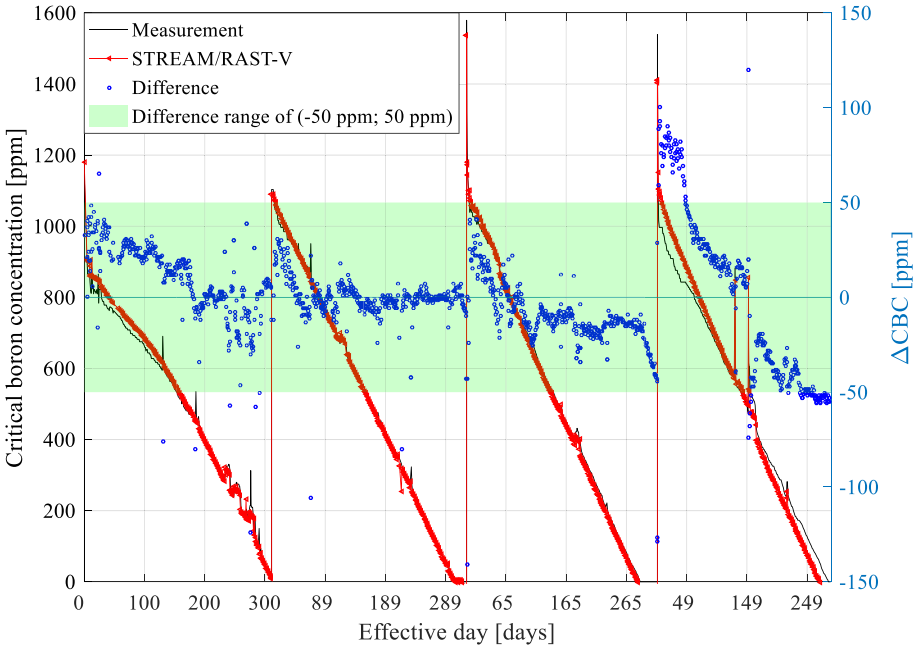

Fig. 15. CBC during four-cycle operations.

other nodal diffusion codes (BIPR7A [9], DYN3D, and TRAPEZ [9]); RAST-V has comparable accuracy.

Fig. 16 shows axial power profiles of cycle 2 at BOC (29 effective days (EFDs)), MOC (105 EFDs), and EOC (218 EFDs). STREAM/RAST-V results are drawn with measurement, and CASMO-4/DYN3D, and BIPR7 [9]. Table 11 summarizes the RMS difference in the axial power profile comparison. The variations of RAST-V calculations compared with measurements are within ±4.88%. Because the number of calculation nodes differ between the two, linear interpolation is applied to compare results. Accordingly, only seven calculation points are used for comparison in each cycle. Compared with other code calculations (BIPR7A with ±3.76% deviation; CASMO-4/DYN3D with ±1.83% deviation), RAST-V computations are worse in BOC. Nevertheless, it has more accurate results in MOC and EOC compared with those of BIPR7A.

4.4. CR worth

Safety analysis, transient calculations, and core condition computations are critical. Moreover, because CR bank (CRB) 10 is used to adjust the reactor reactivity during depletion, assessing the CR calculation capability is also crucial. Fig. 17 presents the CR positions and axial compositions. Ten CRBs are located in the core; Dy_2O_3–TiO_2 and B_4C are composed of CRs.

The BOC HZP condition is used for calculations in the first to fourth cycles of X2 reactor, and the BOC HZP conditions of cycles 1–4 are used for comparison.

Fig. 18 shows the rod worth at cycle 1 under the BOC HZP condition with Serpent 2 calculations; Serpent 2 results and measurements are found in Ref. [7]. In Fig. 18, $\Delta\rho$ is the differential rod worth due to the change of CR positions; the summation of $\Delta\rho$ is the

Table 10
RMS difference of CBC (g/kg) with various code systems.

Cycle	STREAM/RAST-V	BIPR7A	Nessel/DYN3D	CASMO-4/DYN3D	Helios/DYN3	TRAPEZ
1	0.13 (= 23 ppm)	0.29	0.35	0.54	0.24	0.29
2	0.06 (= 11 ppm)	0.47	0.42	0.40	0.33	0.32
3	0.11 (= 20 ppm)	0.48	–	0.39	0.35	0.24
4	0.27 (= 47 ppm)	0.63	–	0.88	0.86	0.79

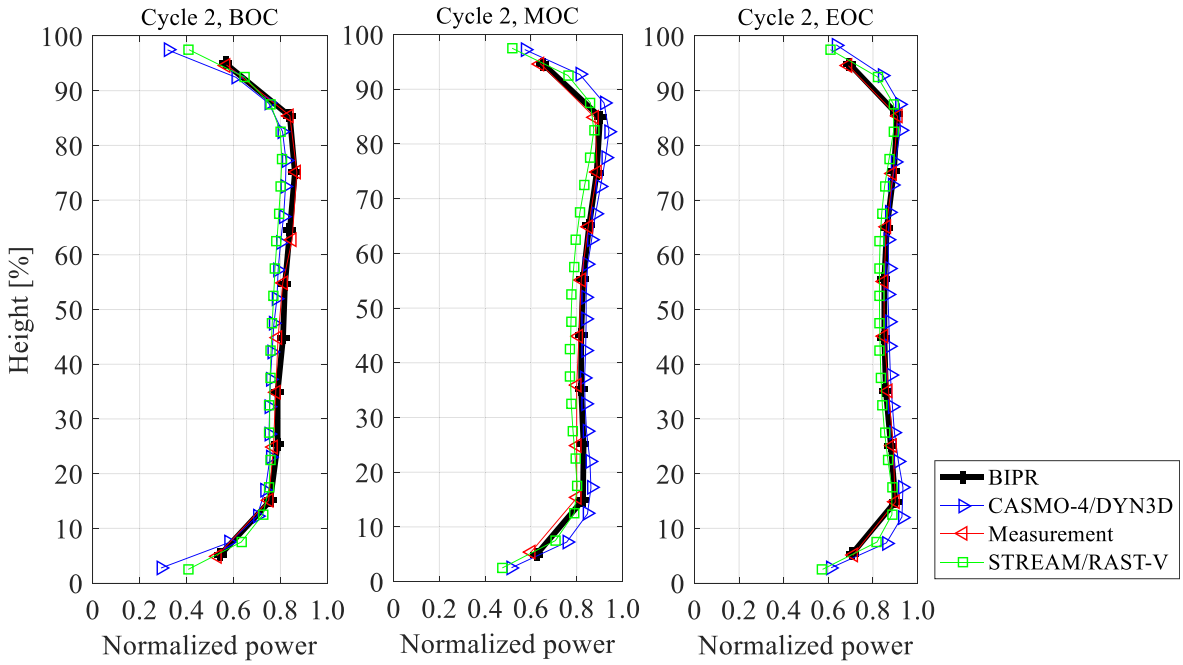

Fig. 16. Axial power profile at cycle 2.

Table 11
RMS difference of axial power profile at cycle 2.

	BOC (29 EFDs)	MOC (105 EFDs)	EOC (218 EFDs)
STREAM/RAST-K	4.88[a]	3.16	2.69
BIPR7A	3.65	3.76	3.36
CASMO-4/DYN3D	1.83	1.28	1.09

[a] Is difference compared with measurements from Ref. [7].

integrated rod worth. Fig. 19 presents the validation results compared with measurements. The accuracy of all calculation results is comparable to that of measurements. Calculations are performed under the BOC HZP condition of each cycle. Table 12 summarizes the CR worth information of each calculation. The variations are within ±79 pcm, and all results are within the 100-pcm criterion set by the Korea Institute of Nuclear Safety [2,48].

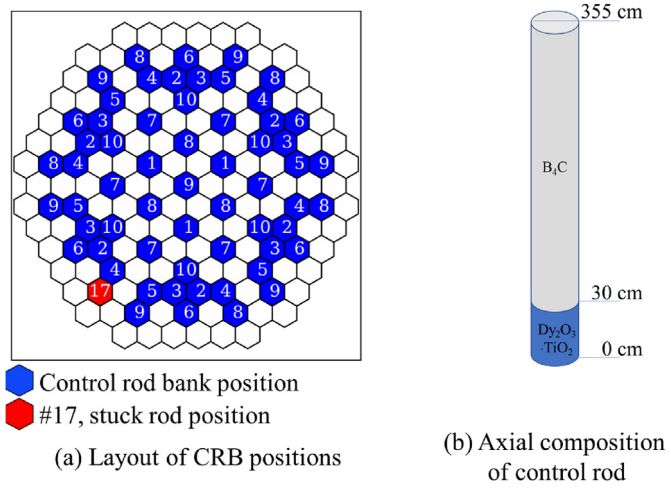

Fig. 17. CR positions.

4.5. SCRAM worth

The SCRAM worth is calculated and compared with Serpent 2 [7], and is important for safety analysis; for instance, SCRAM occurs in a rod ejection accident. Calculation is performed under two different conditions: (1) SCRAM worth considered as a "stuck" rod, and (2) full SCRAM worth. The first calculation is performed to drop all CRs into the lowest positions of the core without a stuck rod. Accordingly, CR #17 was selected as the stuck rod; the CR position is shown in Fig. 17 [7]. In the full SCRAM rod worth calculation, all CRs are dropped to the bottom of the active height (*i.e.*, the stuck rod also drops in this case). In the SCRAM worth calculation, the initial CR positions are located at the top of the active height, and moderator temperature as well as boron concentration conditions are fixed. Table 13 summarizes the critical boron concentration used in the SCRAM worth calculation; the difference is 5 ppm. Table 14 presents the calculated SCRAM worth; the variations are within $\pm 2\sigma$ of the error boundary (*i.e.*, ±53 pcm difference with respect to Serpent 2, and ±596 pcm difference compared with measurements).

4.6. Integrated temperature coefficient

To adjust the calculation capability under HZP conditions, the integrated temperature coefficient (ITC) is calculated and compared with measurements obtained from Ref. [49]. Table 15 contains the calculation results and criterion. Calculation of cycle 1 is performed with 280.4 °C and 276.0 °C. Cycle 2 to cycle 4 calculations is performed with 277 °C–281 °C temperature conditions. Those temperature conditions are consulted from the cycle 2 operation conditions described in Ref. [50]. The criterion is set as 9 pcm, based on Refs. [2,48,49]. All calculation cases are within the criterion boundary (criterion is set as 9 pcm/°C based on Ref. [48]).

5. Verification of transient hexagonal nodal solver

This section presents the transient calculation results using AER-DYN-001 and AER-DYN-002 benchmark problems with different

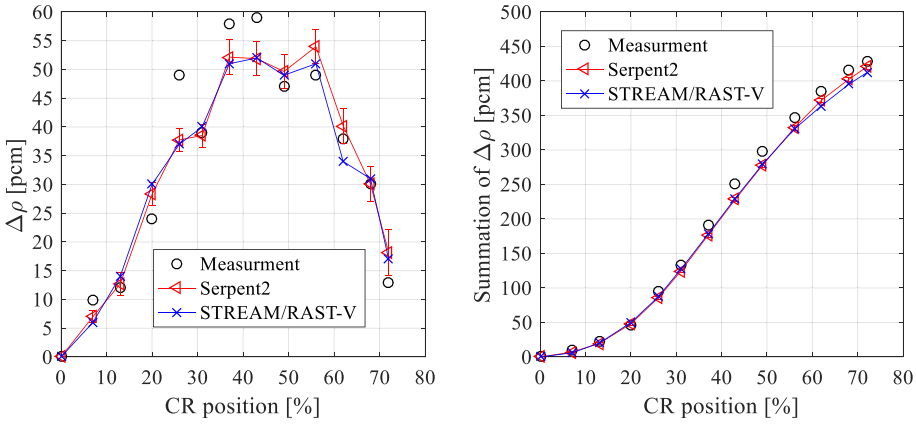

Fig. 18. Rod worth (differential and integrated rod worth) at cycle 1 under BOC HZP.

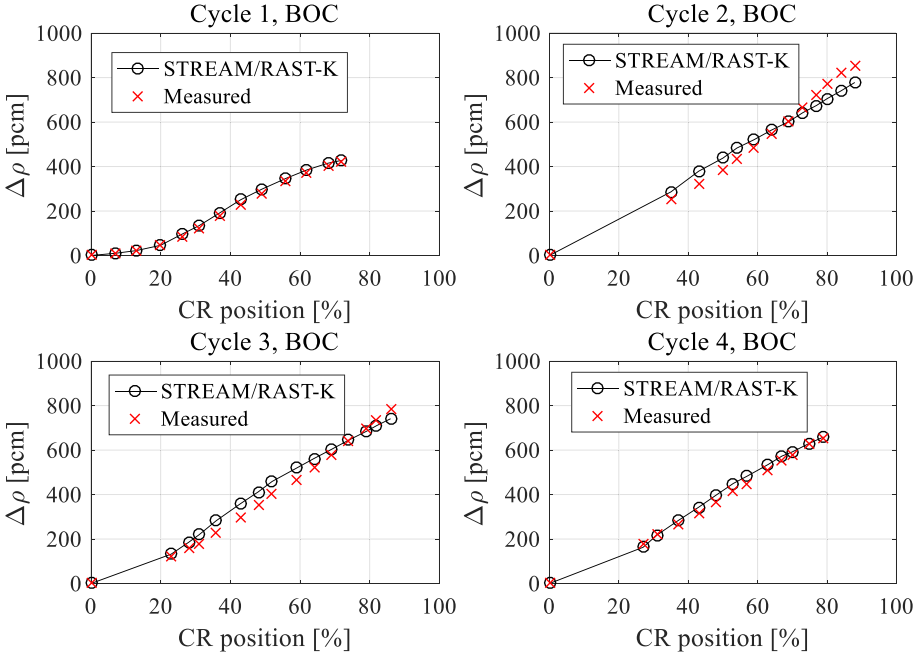

Fig. 19. CR worth at BOC HZP condition (Integrated CR worth).

Table 12
CR worth at BOC HZP.

Cycle 1		Cycle 2		Cycle 3		Cycle 4		Criteria
H10[a] (%)	Diff[b]. (pcm)	H10 (%)	Diff. (pcm)	H10 (%)	Diff. (pcm)	H10 (%)	Diff. (pcm)	100[c] pcm/°C
7	1	35	35	23	10	27	−18	
13	0	43	58	28	27	31	−2	
20	−2	50	53	31	38	37	15	
26	−1	54	48	36	56	43	26	
31	−3	59	36	43	61	48	33	
37	−2	64	16	48	61	53	36	
43	−2	69	−3	52	55	57	33	
49	−1	73	−23	59	50	63	28	
56	2	77	−47	64	39	67	23	
62	8	80	−64	69	25	70	13	
68	7	84	−81	74	7	75	5	
72	8	88	−78	79	−15	79	5	
				82	−25			
				86	−42			

[a] Is axial location of CRB 10 where percent height is calculated by centimeter height using Equation (1).
[b] Is calculated−measured values with measured value obtained from Ref. [9].
[c] Is from Ref. [48].

Table 13
CBC used in SCRAM worth comparison.

Parameter	Measured[a] [A]	STREAM/RAST-K [B]	Serpent 2[b] [C]	Difference ([B] − [A]) (ppm)	Difference ([C] − [A]) (ppm)
CBC (ppm)	1207	1212	1208	5	1

a and b are referred to [7].

Table 14
SCRAM worth.

Reactor state	$\Delta\rho_{measured}$ (pcm) [A]	$\Delta\rho_{STREAM/RAST-K}$ (pcm) [B]	$\Delta\rho_{Serpent2}$ (pcm) [C]	Difference ([B] − [A]) (pcm)	Difference ([B] − [C]) (pcm)
SCRAM with #17 at 100%	5230 ± 310	5803	5750 ± 2	573 ± 310	53 ± 2
Full SCRAM	7000 ± 430	7596	7570 ± 1	596 ± 310	26 ± 1

Table 15
Integrated temperature coefficient results.

Cycle #	H7[a] (%)	H8[b] (%)	H9[c] (%)	H10[d] (%)	CBC [ppm]		ITC (pcm/°C)			Criteria
					C[e]	Diff.[f]	M[g]	C	Diff.	
1	0	0	0	76	1185	5	−6.7	−6.59	0.09	9 pcm/°C
	80	31	100	100	1044	30	−18.6	−13.89	4.71	
2	0	0	0	30	-[h]		−10.5	−6.00	4.50	
	0	0	0	83			−4.3	−2.80	1.50	
3	0	0	0	30			−11.6	−9.25	2.35	
	0	0	0	80			−9.3	−6.40	2.90	
4	0	0	0	33			−15.4	−12.51	2.89	
	0	0	0	78			−12.0	−9.60	2.40	

a, *b*, *c*, and *d* are positions of control rod bank 7, 8, 9, and 10. Details are consulted from Ref. [50]. The notation of 0 is the fully out and 100 is fully inserted.
[e] Is the calculated value by STREAM/RAST-K.
[f] Is the difference between calculated value and measurement.
[g] Is the measurement. References are consulted from Refs. [2,48,50].
[h] Is that the reference does not provide by specification.

rod ejection accident scenarios: low power change transient, and extreme rod ejection transient. VVER-440 model is used for transient calculation. Boron steel is used for absorber part of control assemblies in VVER-440 [51], and control rod model is composed by bar to drive region and absorber part [52]. Control rod is fully designed with one material in this calculation.

5.1. AER-DYN-001

Fig. 20 presents the radial layout of the VVER reactor used for the analysis of AER-DYN-001 and AER-DYN-002; the axial compositions of CRs are also presented in this figure. The active height is 250 cm, and CR1 and CR2 are inserted into the core in the initial state; CR1 and CR2 are CRBs 1 and 2, and SR1 and SR2 are shutdown rod banks 1 and 2, respectively. Rods CR1 and CR2 are located 50 cm from the bottom of the active height. In the calculation, lower part of 50 cm uses the FA cross sections instead of CR cross sections. Rod ejections are performed from 0.00 to 0.08 s. The yellow CR position (CR2) is used for the CR ejection scenario. The calculated time period is set as 0−2 s, and the time step size is set as 0.01 s. At 0.08 s, SCRAM is performed with 23 and 25 CRBs. The detailed calculation scenario is presented in Fig. 21 (b). The axial reflector thickness is 25 cm, and the core consists of four different materials. The macroscopic cross-section used for calculation is presented in Ref. [10]. Twelve calculation nodes are used axially: the active height region has 10 calculation nodes, and the bottom and top reflector regions each has one node. Table 16 lists the main calculation conditions used for AER-DYN-001 and AER-DYN-002 benchmarks [10,11]. A total of 349 FAs is loaded into the core, and three types of FAs are used. To maintain the consistency of calculation conditions, the T/H feedback is ignored in this computation. Fig. 21 presents the calculation results compared with other nodal diffusion codes [10,25]. The trend of RAST-V is similar to the BKM and TRIKIN code systems.

5.2. AER-DYN-002

This section presents the calculation results of AER-DYN-002 benchmark, which is under extremely changed power conditions during a rod ejection accident. Table 17 contains the summary of the AER-DYN-002 benchmark calculation conditions. To maintain the calculation conditions described in Ref. [11], Doppler feedback is considered. As reported in a previous study, because the coolant temperature does not undergo T/H feedback, the gap conductance is set as 0.1 J/m^2•°C (approximately 0) [54]. Hence, only the Doppler temperature feedback is considered in this calculation. Equation (10) is used for the macroscopic cross-section feedback [11]:

$$\Sigma_{f,2}^{n}(t) = \Sigma_{f,2}^{n,0}\left[1+\gamma\left(\sqrt{T_f^n(t)}-\sqrt{T_{f,0}}\right)\right], \tag{10}$$

where $\Sigma_{f,2}^{n}(t)$ is the macroscopic fission cross-section in the nth node; n is the node index, and 2 is the energy group number (1 and 2 are the fast group and thermal group, respectively); $\Sigma_{f,2}^{n,0}$ is the initial macroscopic fission cross-section; $T_{f,0}$ is the initial fuel temperature (260 °C); $T_f^n(t)$ is the fuel temperature in the nth node; and γ is -7.228×10^{-4} (°C)$^{-1/2}$. At 0 s, the core is under the HZP condition; thus, the initial fuel temperature and moderator temperature are both 260 °C. The power is 1.375 kW (10^{-5}% of nominal power). Rod ejection is performed from 0 to 0.16 s, and a yellow CR is ejected at this period; the yellow CR positions are presented in Fig. 20. The control rod velocity is set as 12.5 m/s.

Fig. 22 presents the AER-DYN-002 calculation results, and BIPR8 and DYN3D are used for code-to-code comparison. Various code

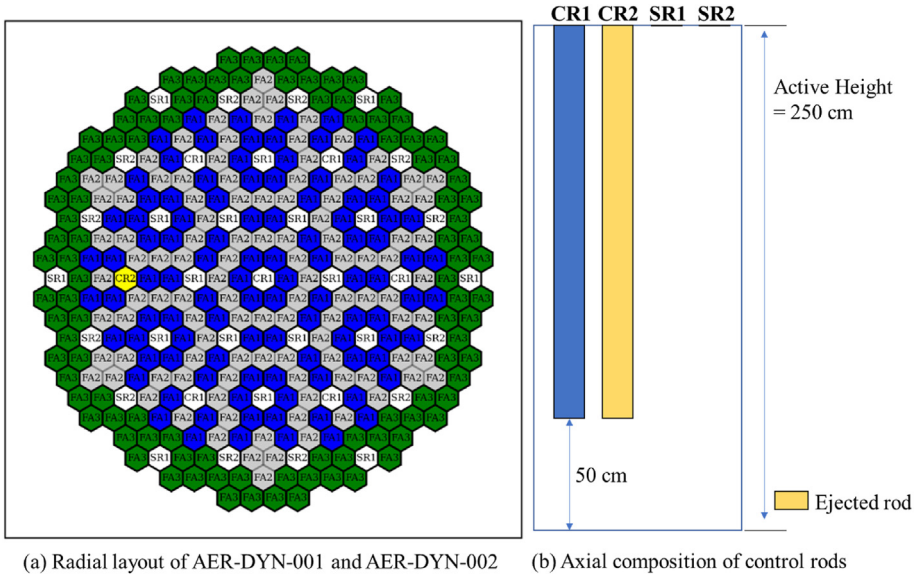

Fig. 20. Radial layout of AER-DYN-001 and AER-DYN-002 cases.

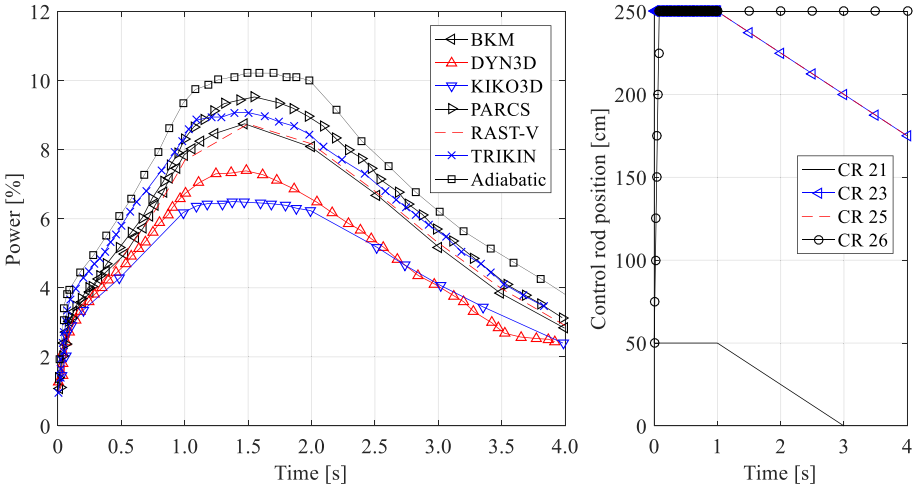

Fig. 21. Rod ejection results.

Table 16
Calculation condition of AER-DYN-001.

Parameter	Contents	Unit	Reference
Reactor type	VVER-440		[10,11]
Nominal power	1375[a]	MWth	[53]
Fuel pitch	14.7	cm	[10,11]
Active height	250	cm	
Axial node	24 (2 reflector regions and 22 fuel regions)		
Number of FAs	349		
CR height	250	cm	Assumption[b]

[a] Is nominal power referred to KOLA reactor.
[b] Is set as active height.

results are obtained from Refs. [10,54]. The initial CR position is 50 cm from the bottom region of the active core height. The control rod position is the same as that shown in Fig. 20, and RAST-V results have comparable accuracies, as shown in the Fig. 22. The power and integrated power conditions are compared as functions of the simulation time. As shown on the left-hand graph, the power conditions caused by rod ejection and calculated by RAST-V exhibit a trend similar to those of HEXTRAN and BIPR8. In addition, in comparing the integrated power condition, the accuracy of RAST-V is observed to be comparable to that of BIPR8.

6. Verification of SNF module

A spent-fuel analysis module has been developed for the back-

Table 17
Calculation condition of AER-DYN-002 case.

Parameter	Contents	Unit	Reference
Velocity	12.5	m/s	[11]
Period of rod ejection	0–0.16	s	
Initial power condition at HZP	1.375[a] (10^{-5}% of nominal power)	kW	
Initial position of CR	50	cm	
Ejected rod position	26[b]		
# of pins per FA	126		

[a] Nominal power is referred to Ref. [11].
[b] CR position is presented in Fig. 20.

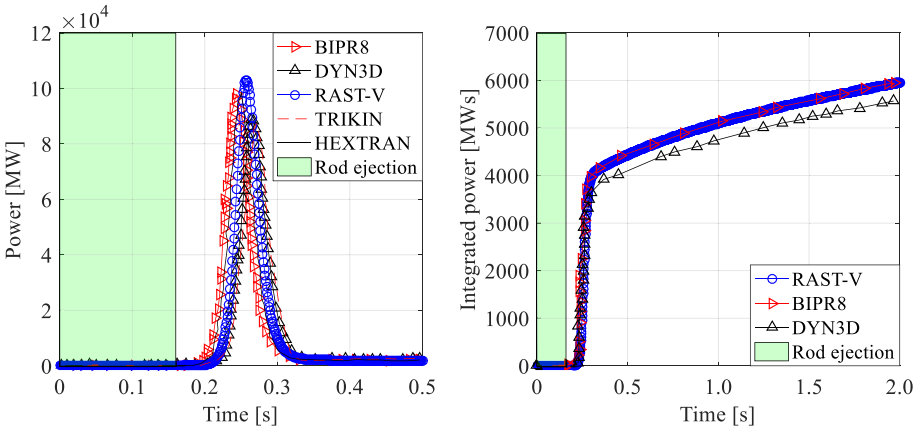

Fig. 22. AER-DYN-002 results with various code systems.

end cycle analysis. This section presents the V&V results of the SNF analysis module, which is implemented based on the equations presented in Section 2.4. The SNF module was developed based on Lagrange interpolation and CRAM of 36 isotopes, and V&V was performed with a pin sample (ID = 21) discharged from Novovoronezh-4 [12]. The samples were measured by the Lawrence Livermore National Laboratory. Novovoronezh is a VVER-440 reactor, and the ENDF/B-VII.0 neutronics library is used for the calculation. The discharged burnup of the sample was 41.50 MWd/kg and underwent 15–18 cycles before discharging; the up-time was 1109 days. The active height of FA is 244 cm, pin pitch is 1.22 cm, FA pitch is 14.7 cm, and shroud thickness is 0.40 cm. Fig. 23 shows the radial and axial layouts of FA. In subplot (a), the pin sample location is yellow, and its axial location is 100 cm from the active height. Fig. 23 (a) also shows one central guide tube, and 126 UO_2 fuel pins are located in the FA model. The FA model was used to calculate the reflective boundary.

Fig. 24 presents the operating condition history for the calculation, specifically fuel temperature, moderator temperature, boron concentration, and power density. The calculation conditions are presented in Ref. [12], which presents the boron concentration in g_{H3BO3}/kg_{H2O}. A constant of 174.88 ppm/(g_{H3BO3}/kg_{H2O}) is applied to convert the boron concentration found in Ref. [7]. A specific calculation condition is used for each time step.

Fig. 15 shows the calculated results of 38 isotopes. The calculation is performed as follows. (1) The number density file is generated by STREAM through history branch calculation. (2) A 3D core simulation is performed by RAST-V (generation of simulation condition history) and isotope number density is calculated by Lagrange interpolation with history indices reflected 3D core simulation conditions. (3) Cooling and source term calculations (*e.g.*, decay heat) are performed. Different cooling periods are used to calculate each isotope. The standard deviation of measurements is derived from Ref. [12]. As shown in a previous study [39,43], compared with the one-step method (lattice code calculation), this approach benefits simulation because it reduces the simulation time due to the additional source term calculation code.

Table 18 lists the detailed relative differences among isotopes in terms of composition. Compared with the measured uncertainty, most of the isotopes are within the ±1 σ boundary; five isotopes are located on the boundary. In addition, most of the isotopes exhibit a trend similar to the CASMO-4E results. In particular, RAST-K provides more accurate isotope results for ^{134}Cs, ^{147}Sm, ^{151}Sm, and ^{109}Ag.

Fig. 25 presents the validation results with measurements and those of CASMO-4E. The CASMO-4E results are calculated with the ENDF/B-VI.0 library, as shown in Ref. [55]; the measurement is from Ref. [12]. RAST-V has comparable accurate results, as summarized in Table 18.

7. Conclusion

The VVER analytic solver was developed and adopted in the in-house nodal diffusion code, RAST-K. The main calculation features were presented using V&V calculations performed with Rostov-II, X2, Novovoronezh-4, and AER benchmarks. Five main features were verified and validated in this study: depletion, T/H feedback, multicycle operation, transient calculations, and spent-fuel analysis.

The micro-depletion scheme was verified with Rostov-II U22 FA. The analysis results of 36 isotopes were within ±50 pcm compared with those of lattice code STREAM. To assess the calculation capability of multicycle operation, the X2 benchmark was used; cycles 1–4 were used for comparison. The RMS difference of each cycle was within ±47 ppm in the four-cycle operation. The CR worth was calculated under 50 different calculation conditions. The variations were within ±81 pcm in all multicycle calculations, and all calculation cases were within the criteria provided by the Korean

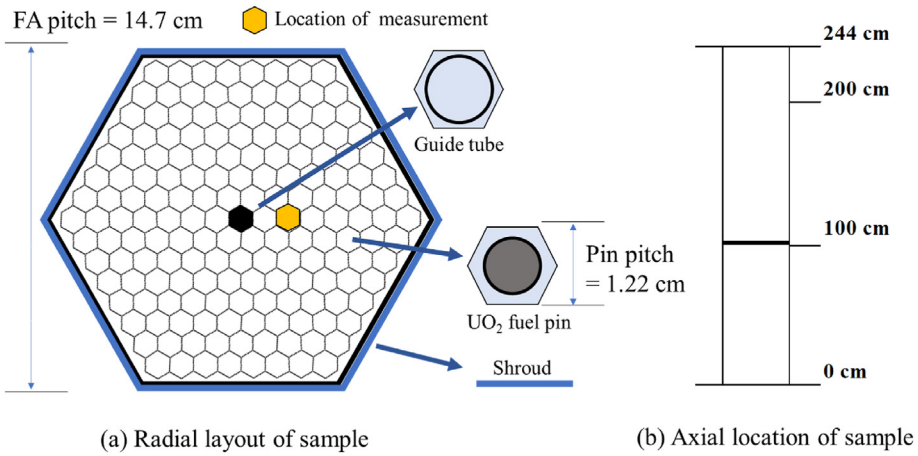

Fig. 23. Radial and axial layout of the FA.

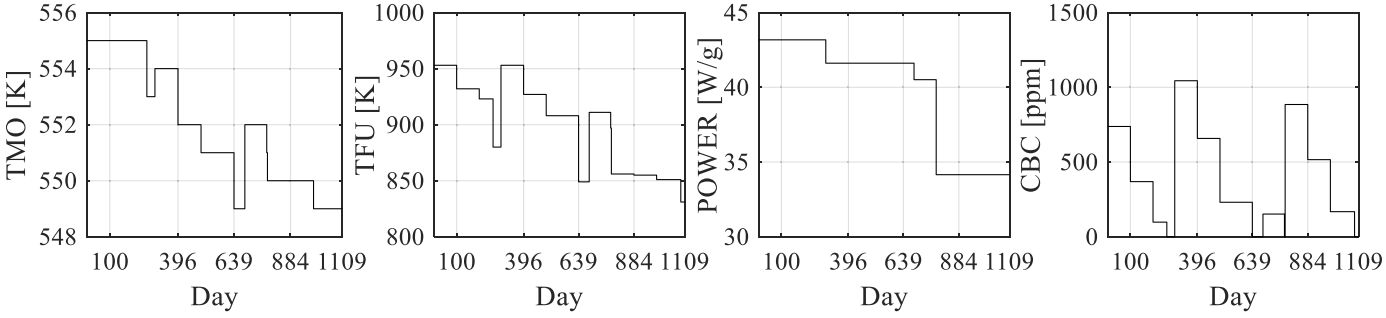

Fig. 24. Operating condition.

Table 18
Relative difference of Isotope composition.

Isotope	C^k/E^l-1 (%)	$\sigma_{measured}$ (%)	Isotope	C/E−1 (%)	$\sigma_{measured}$ (%)	Isotope	C/E−1 (%)	$\sigma_{measured}$ (%)
$^{234}U^a$	−17.14	47	$^{245}Cm^d$	−0.22	9	$^{142}Ce^e$	−8.96	50
$^{235}U^b$	2.86	28	$^{246}Cm^d$	7.92	4	$^{147}Sm^e$	0.74	50
$^{236}U^b$	−6.12	28	$^{142}Nd^c$	−8.65	9	$^{148}Sm^e$	6.62	33
$^{238}U^b$	−0.39	37	$^{143}Nd^c$	−7.88	9	$^{149}Sm^e$	46.78	10
$^{237}Np^a$	−55.70	10	$^{144}Nd^c$	−9.48	10	$^{150}Sm^e$	0.46	55
$^{238}Pu^b$	31.17	24	$^{145}Nd^c$	−18.40	9	$^{151}Sm^e$	15.95	25
$^{239}Pu^b$	11.99	14	$^{146}Nd^c$	−0.33	8	$^{152}Sm^e$	−5.01	20
$^{240}Pu^b$	5.80	10	$^{148}Nd^c$	3.58	5	$^{154}Sm^e$	6.47	22
$^{241}Pu^b$	3.14	12	$^{150}Nd^c$	−8.10	2	$^{95}Mo^f$	−10.53	17
$^{242}Pu^b$	−8.38	5	$^{133}Cs^d$	−3.61	46	$^{99}Tc^f$	−7.96	17
$^{241}Am^c$	14.66	17	$^{134}Cs^d$	−5.90	6	$^{101}Ru^i$	−8.54	18
$^{242m}Am^c$	−58.18	10	$^{135}Cs^d$	−13.61	19	$^{105}Pd^j$	−9.19	96
$^{243}Am^c$	20.48	87	$^{137}Cs^d$	−5.75	50	$^{108}Pd^j$	29.62	26
$^{244}Cm^d$	18.21	36	$^{140}Ce^e$	−8.25	50	$^{109}Ag^j$	34.23	15

Cooling time of *a*, *b*, *c*, *d*, *e*, *f*, *i*, and *j* are 0, 12.397, 12.408, 12.359, 12.414, 12.427, 12.403, 12.419, and 12.433 years, respectively; *k* and *l* are calculated and measured values, separately.

Institute of Nuclear Safety. The integrated temperature coefficients were also compared under the HZP condition, and the variations in the ITC calculations were also within the criteria of 9 pcm/°C. The AER-DYN-001 and AER-DYN-002 benchmark problems were used to verify the transient calculation, and RAST-V yielded reasonable results compared with various code systems. Novovoronezh-4 was used to validate the spent-fuel analysis module. Most of the isotope results were within one-standard deviation boundary of measurements.

The RAST-V code system provides accurate results comparable to those of steady-state calculations, transient calculations, and additional applications. This paper introduces the newly developed nodal diffusion code and demonstrates the V&V of RAST-V. In future work, back-end cycle analysis will be performed using the cask model.

Declaration of competing interest

The authors declare the following financial interests/personal relationships which may be considered as potential competing interests:

There are no known conflicts of interest associated with this paper. This work was supported by the National Research Foundation of Korea (NRF) grant funded by the Korea government

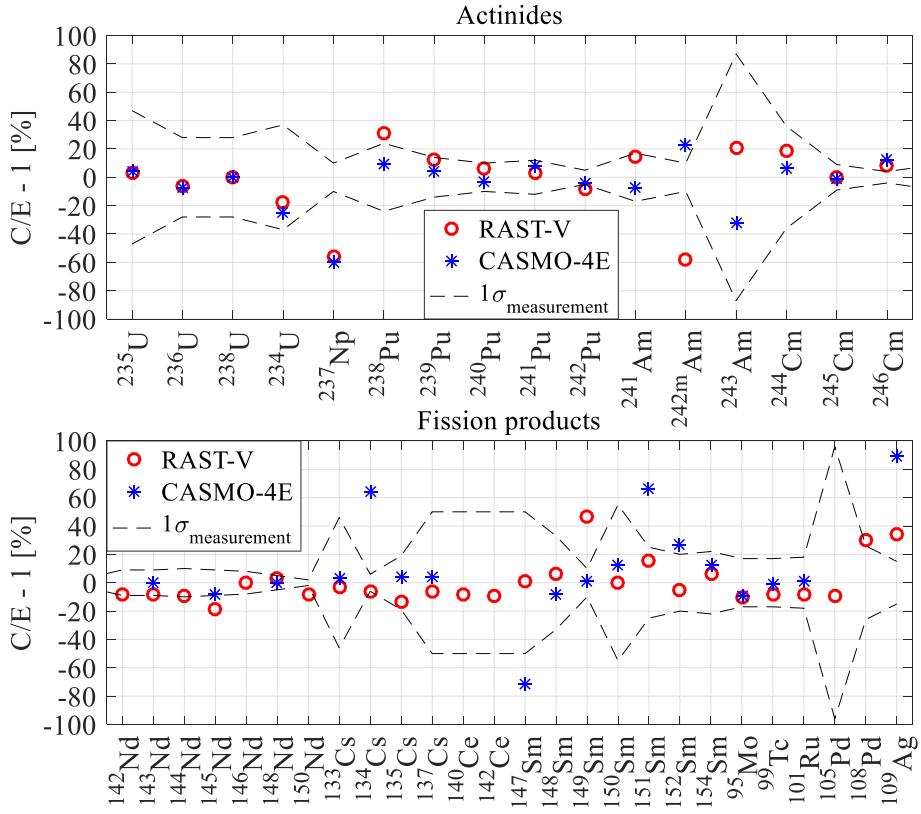

Fig. 25. Relative difference of sample 21 calculation.

(MSIT). (No.NRF-2017M2A8A2018595)

I am one author signing on behalf of all co-author of the manuscript.

Acknowledgments

This work was supported by the National Research Foundation of Korea (NRF) grant funded by the Korea government (MSIT). (No.NRF-2017M2A8A2018595)

Appendix

This section contains the details of neutron sources from the axial NEM to the radial TPEN method. Figure A. 1 shows the notations of variables used in the axial and radial calculations. Subplot (a) presents the variables used in axial NEM calculation. Subplot (b) contains the variables used to calculate the radial leakage term based on the axial leakage source. Subplot (c) contains the unknowns used in TPEN solver.

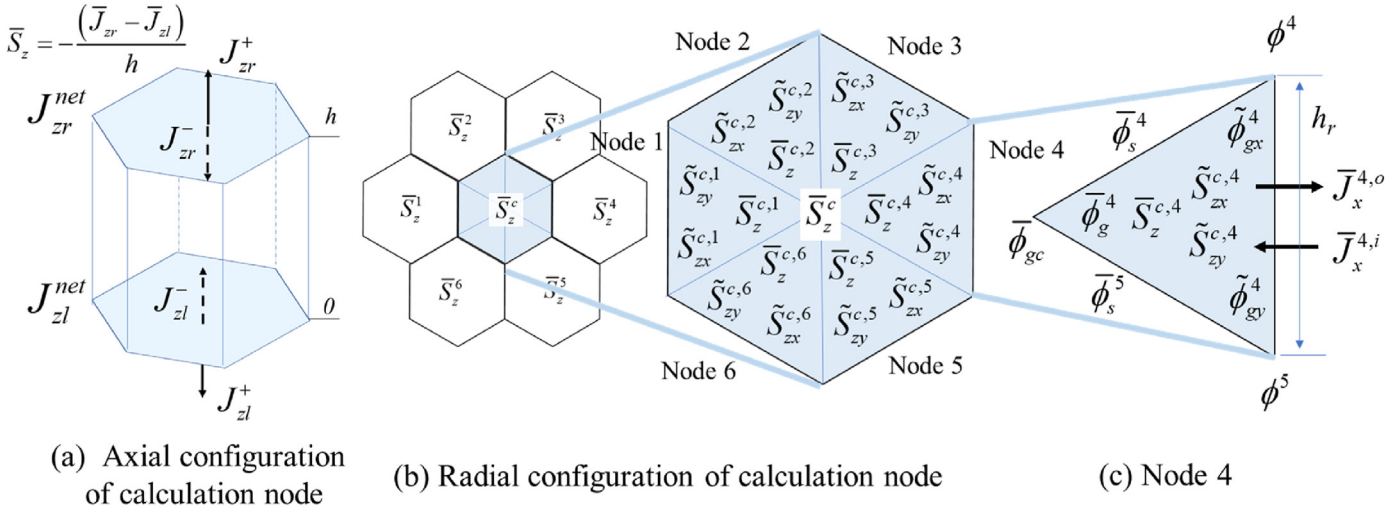

Fig. A. 1 Variables for 1D NEM and 2D TPEN calculations

In NEM solver, the 4th and 2nd order polynomials are used for flux and leakage term as shown in equation (A.1) and (A.2), separately.

$$\phi_g^m(\xi) = \overline{\phi}_g^m + \sum_{i=1}^{4} a_{i,g}^m P_i(\xi), \tag{A.1}$$

$$L_g(\xi) = L_{avg,g} + e_{1,g}P_1(\xi) + e_{2,g}P_2(\xi), \tag{A.2}$$

where ξ is the z divided by h (normalization): h is the axial node size, and $a_{i,g}$ is the coefficient: $a_{1,g}$ and $a_{2,g}$ are easily find by using boundary conditions at 0 and h in axial direction. The notation of L_g is the leakage term, g is the energy group number ($g = 1, 2$ due to generally two-group constants are used for VVER analysis), m is axial node index, the P_i is the basis of polynomial: $P_1(\xi) = 2\xi - 1$, $P_2(\xi) = 6\xi(1-\xi) - 1$, $P_3(\xi) = 6\xi(1-\xi)(2\xi - 1)$, $P_4(\xi) = 6\xi(1-\xi)(5\xi^2 - 5\xi + 1)$. The coefficients of $a_{1,g}$ and $a_{2,g}$ are defined as equation (A.3), and $a_{3,g}$ and $a_{4,g}$ are defined as equation (A.4).

$$\begin{aligned} a_{1,g} &= J_{zr,g}^{+} + J_{zr,g}^{-} - J_{zl,g}^{+} - J_{zl,g}^{-} \\ a_{2,g} &= \overline{\phi}_g^m - J_{zr,g}^{+} - J_{zr,g}^{-} - J_{zl,g}^{+} - J_{zl,g}^{-}, \end{aligned} \tag{A.3}$$

$$\begin{aligned} \tilde{\phi}_{1,g}^m &= \int_0^1 P_1(\xi)\phi_g^m(\xi)d\xi = \frac{1}{3}a_{1,g} + \frac{1}{5}a_{3,g} \\ \tilde{\phi}_{2,g}^m &= \int_0^1 P_2(\xi)\phi_g^m(\xi)d\xi = \frac{1}{5}a_{2,g} - \frac{3}{35}a_{4,g}, \end{aligned} \tag{A.4}$$

where $J_{zr,g}^{+}$ and $J_{zr,g}^{-}$ are outgoing and incoming current at h, respectively. The $J_{zl,g}^{+}$ and $J_{zl,g}^{-}$ are outgoing and incoming current at 0. To calculate the outgoing current, equation (A.5) is used for calculation.

$$\begin{aligned} J_{zr,g}^{net} &= -\beta_g \frac{d\phi_g^m(\xi)}{d\xi}\Big|_{\xi=1} = -2\beta_g(a_{1,g} - 3a_{2,g} - 3a_{3,g} - 3a_{4,g}) \\ &= J_{zr,g}^{+} - J_{zr,g}^{-} J_{zl,g}^{net} = -\beta_g \frac{d\phi_g^m(\xi)}{d\xi}\Big|_{\xi=0} \\ &= -2\beta_g(a_{1,g} + 3a_{2,g} - 3a_{3,g} + 3a_{4,g}) \\ &= J_{zl,g}^{-} - J_{zl,g}^{+}, \end{aligned} \tag{A.5}$$

where $J_{zr,g}^{net}$ and $J_{zl,g}^{net}$ are net current at h and 0, β_g is D_g divided by h. Outgoing current equation is simplified as equation (A.6).

$$\begin{aligned} J_{zr,g}^{+} &= c_{1,g}J_{zr,g}^{-} + c_{2,g}J_{zl,g}^{-} + c_{3,g}\overline{\phi}_g + c_{4,g}\tilde{\phi}_{1,g} + c_{5,g}\tilde{\phi}_{2,g} \\ J_{zl,g}^{+} &= c_{2,g}J_{zr,g}^{-} + c_{1,g}J_{zl,g}^{-} + c_{3,g}\overline{\phi}_g - c_{4,g}\tilde{\phi}_{1,g} + c_{5,g}\tilde{\phi}_{2,g}, \end{aligned} \tag{A.6}$$

where coefficients ($c_{1,g}$ to $c_{5,g}$) are presented in equation (A.7).

$$\begin{aligned} c_{1,g} &= \left(-\frac{960\beta_g{}^2 - 1}{960\beta_g{}^2 + 64\beta_g + 1}\right), c_{2,g} = \left(-\frac{16\beta_g}{960\beta_g{}^2 + 64\beta_g + 1}\right), \\ c_{3,g} &= \left(\frac{20\beta_g}{40\beta_g + 1}\right), \quad c_{4,g} = \left(\frac{30\beta_g}{24\beta_g + 1}\right), c_{5,g} = \left(-\frac{70\beta_g}{40\beta_g + 1}\right) \end{aligned} \tag{A.7}$$

To calculate the coefficient of $a_{3,g}$ and $a_{4,g}$ nodal balance equation, 1st momentum, and 2nd momentum equations are used. Equation (A.8) is used to calculate the fluxes and those calculated fluxes and momentums are utilized to insult into the equation (A.6) to calculate the outgoing current.

$$\begin{bmatrix} g_1 & 0 & 0 & 0 & g_3 & 0 \\ 0 & g_2 & 0 & 0 & 0 & g_4 \\ 0 & 0 & g_5 & g_6 & 0 & 0 \\ 0 & 0 & g_7 & g_8 & 0 & 0 \\ g_9 & 0 & 0 & 0 & g_{11} & g_6 \\ 0 & g_{10} & 0 & 0 & g_7 & g_{12} \end{bmatrix} \begin{bmatrix} \overline{\phi}_1 \\ \overline{\phi}_2 \\ \tilde{\phi}_{1,1} \\ \tilde{\phi}_{1,2} \\ \tilde{\phi}_{2,1} \\ \tilde{\phi}_{2,2} \end{bmatrix} = \begin{bmatrix} src_{1,1} \\ src_{1,2} \\ src_{2,1} \\ src_{2,2} \\ src_{3,1} \\ src_{3,2} \end{bmatrix}$$

$$\begin{aligned} &g_1 = \frac{40\beta_1}{h} - \frac{80\beta_1 c_{3,1}}{h} + \Sigma_{r,1}, g_2 = \frac{40\beta_2}{h} - \frac{80\beta_2 c_{3,2}}{h} + \Sigma_{r,2}, g_3 = -\frac{80\beta_1 c_{5,1}}{h} - \frac{140\beta_1 c_{5,1}}{h} \\ &g_4 = -\frac{80\beta_2 c_{5,2}}{h} - \frac{140\beta_2 c_{5,2}}{h}, g_5 = \frac{1}{h}(60\beta_1 - 40\beta_1 c_{4,1}) + \Sigma_{r,1} - \lambda\nu\Sigma_{f,1}, g_6 = -\lambda\nu\Sigma_{f,2}, g_7 = -\Sigma_s \\ &g_8 = \frac{1}{h}(60\beta_2 - 40\beta_2 c_{4,2}) + \Sigma_{r,2}, g_9 = \frac{56\beta_1 c_{3,1} - 28\beta_1}{h}, g_{10} = \frac{56\beta_2 c_{3,2} - 28\beta_2}{h} \\ &g_{11} = \frac{140\beta_1}{h} + \frac{56\beta_1 c_{5,1}}{h} + \Sigma_{r,1} - \lambda\nu\Sigma_{f,1}, g_{12} = \frac{140\beta_2}{h} + \frac{56\beta_2 c_{5,2}}{h} + \Sigma_{r,2} \end{aligned} \tag{A.8}$$

where $src_{1,g}$, $src_{2,g}$, and $src_{3,g}$ are constants which don't have relationship with $\bar{\phi}_g$, $\tilde{\phi}_{1,g}$, and $\tilde{\phi}_{2,g}$. Those constants are calculated by nodal balance, 1st momentum, and 2nd momentum equations. Calculated outgoing current is used to calculate the axial leakage source as shown in equation (A.9).

$$\bar{S}_z = -\frac{1}{h}(\bar{J}_{zr} - \bar{J}_{zl}), \tag{A.9}$$

This axial leakage source is used to calculate the radial leakage sources used in 2D TPEN calculation solver [33].

$$\bar{S}_z^{c,n} = \frac{1}{A}\int_A S_z(x,y)dA\tilde{S}_{zx}^{c,n} = \frac{2}{\sqrt{3}h_r}\frac{1}{A}\int_A xS_z(x,y)dA\,\tilde{S}_{zy}^{c,n} = \frac{2}{h_r}\frac{1}{A}\int_A yS_z(x,y)dA \tag{A.10}$$

where A is the radial hexagonal node, and h_r is the side length of the hexagonal as presented in subplot (c) of Figure A. 1. The positions of the radial leakage source are presented in subplot (b) of Figure A. 1. Equation (A.11) are used for calculation [33]:

$$\begin{aligned}
\bar{S}_{gz}^{c,n} &= w_1 S_{gz}^{c} + w_2 S_{gz}^{n} + w_3\left(S_{gz}^{n+1} + S_{gz}^{n+5}\right) + w_4\left(S_{gz}^{n+2} + S_{gz}^{n+4}\right) + w_5 S_{gz}^{n+3} \\
\tilde{S}_{gzx}^{c,n} &= w_{x1} S_{gz}^{c} + w_{x2} S_{gz}^{n} + w_{x3}\left(S_{gz}^{n+1} + S_{gz}^{n+5}\right) + w_{x4}\left(S_{gz}^{n+2} + S_{gz}^{n+4}\right) + w_{x5} S_{gz}^{n+3} \\
\tilde{S}_{gzy}^{c,n} &= w_{y1}\left(S_{gz}^{n+1} + S_{gz}^{n+5}\right) + w_{y2}\left(S_{gz}^{n+2} - S_{gz}^{n+4}\right)
\end{aligned} \tag{A.11}$$

where n is the node number. If $n + i > 6$, then $n+i-6$ is used instead of $n+i$ (i is integer). Those sources are used in radial TPEN solver as shown in equation (3) of section 2.1.

Abbreviations

1D	one dimensional
2D	two dimensional
3D	three dimensional
ADF	assembly discontinuity factor
AER	Atomic Energy Research
BA	burnable absorber
BiCGSTAB	Bi-Conjugate Gradient Stabilized
BOC	beginning of cycle
BOR	boron concentration
BWR	boiling water reactor
CBC	critical boron concentration
CDF	corner discontinuity factor
CMFD	coarse mesh finite difference
CR	control rod
CR1	control rod bank 1
CR2	control rod bank 2
CRAM	Chebyshev rational approximation method
CRB	control rod bank
EOC	end of cycle
EFD	effective day
FA	fuel assembly
HZP	hot zero power
NEM	nodal expansion method
MOC	middle of cycle
PSM	pin-based slowing-down method
PWR	pressurized water reactor
RAST-V	RAST-K VVER
RK	RAST-K v2.0
RMS	root mean square
RV	RAST-K VVER
ST	STREAM
SR1	Shutdown bank 1
SR2	Shutdown bank 2
TFU	fuel temperature
T/H	thermal-hydraulic
T/H 1D	simplified one-dimensional single channel thermal hydraulic feedback
TPEN	Triangular-based polynomial expansion nodal method
TMO	moderator temperature
VVER	Vodo–Vodyanoi Energetichesky Reactor
V&V	verification and validation
WT%	weight percent

References

[1] J. Park, J. Jang, H. Kim, J. Choe, D. Yun, P. Zhang, A. Cherezov, D. Lee, RAST-K v2-Three-dimensional nodal diffusion code for pressurized water reactor core analysis, Energies 13 (2020) 6324, https://doi.org/10.3390/en13236324.

[2] J. Choe, S. Choi, P. Zhang, J. Park, W. Kim, H.C. Shin, H.S. Lee, J. Jung, D. Lee, Verification and validation of STREAM/RAST-K for PWR analysis, Nucl. Eng. Technol. 51 (2) (2019) 356–368, https://doi.org/10.1016/j.net.2018.10.004.

[3] J.Y. Cho, C.H. Kim, Development of a Polynomial Expansion Nodal Method for Hexagonal Geometry, Theses of Ph.D., Seoul National University, 1995 https://s-space.snu.ac.kr/handle/10371/51486.

[4] J. Jang, T.T. Quoc, S. Dzianisau, W. Lee, D. Lee, Verification of RAST-K hexagonal analysis module with SNR and VVER-440 benchmarks, KNS Winter Meeting (Dec 16–18, 2020). Korea (online).

[5] J. Jang, A. Chezerov, Y. Jo, T.T. Quoc, S. Dzianisau, W. Lee, J. Park, D. Lee, Verification of RAST-K hexagonal transient solver with OCED/NEA benchmark problem of KALININ-3 NPP, KNS Winter Meeting (Dec 16–18, 2020). Korea (online).

[6] M. Avramova, K. Ivanov, K. Velkov, S. Nikonov, P. Gordienko, B. Shumskiy, O. Kavun, Benchmark on Reactivity Compensation of Boron Dilution by Stepwise Insertion of Control Rod Cluster into the VVER-1000 Core, Version 1.5, OECD Nuclear Energy Agency, March 2020.

[7] Y. Bilodid, E. Fridman, T. Lötsch, X2 VVER-1000 benchmark revision: fresh HZP core state and the reference Monte Carlo solution, Ann. Nucl. Energy 144 (2020), https://doi.org/10.1016/j.anucene.2020.107558.

[8] T. Lötsch, V. Khalimonchuk, A. Kuchin, Corrections and Additions to the Proposal of a Benchmark for Core Burnup Calculations for a Vver-1000 Reactor, 19th AER Symposium, 2010.

[9] T. Lötsch, S. Kliem, E. Bilodid, V. Khalimonchuk, A. Kuchin, Y. Ovdienko, M. Ieremenko, R. Blank, G. Schultz, The x2 benchmark for vver-1000 reactor calculations results and status, in: Novel Vision of Scientific & Technical Support for Regulation of Nuclear Energy Safety: Competence, Transparency, Responsibility, Dedicated to the 25th Anniversary of the SSTC NRS Kiev, Ukraine, March 22–23, 2017.

[10] A. Keresztúri, M. Telbisz, AER Benchmark Specification Sheet AER-DYN-001, AER Benchmark Book, Forschungszentrum Rossendorf, Institute of Safety Research, Dresden, Germany, Oct. 10, 1999.
[11] U. Grundmann, AER Benchmark Specification Sheet AER-DYN-002, AER Benchmark Book, Forschungszentrum Rossendorf, Institute of Safety Research, Dresden, Germany, Oct. 10, 1999.
[12] L. Markova, Simplified benchmark specification based on #2670 ISTC VVER PIE, in: 12th Meeting of AER, Slovakia, April 16–18, 2007.
[13] The VVER Today, ROSATOM, Retrieved May 31, 2018, https://rosatom.ru/upload/iblock/0be/0be1220af25741375138ecd1afb18743.pdf.
[14] Current Status of Russian Nuclear Power Development and Cooperation with Europe: the Issue of Human Resource Development Rosatom Technical Academy, https://enen.eu/wp-content/uploads/2019/08/13-artisiuk_01_03_18_brussel.pdf.
[15] Russian Nuclear Power, 2018. Bellona, P17, https://network.bellona.org/content/uploads/sites/2/2018/08/Russian-Nuclear-Power-2018.pdf.
[16] F.P. Weiss, S. Mittag, Validation of coupled neutron-kinetic/thermal-hydraulic codes against transients measured in VVER reactors, in: Phare SRR-1/95: Final Technical Report FZR/SRR195/FIN2.1, 2000. Brussels, Belgium.
[17] S. Mittag, U. Grundmann, et al., Validation of Coupled Neutronic/Thermal-Hydraulic Codes for VVER Reactors Final Report (FZR–408), 2004. Germany.
[18] AER Benchmark Book, Atomic Energy Research (AER), 1999. Budapest, http://aerbench.kfki.hu.
[19] T. Apostolov, B. Petrov, Operational: Benchmark for VVER-1000, UNIT 5, KOZLODUY NPP, Ninth Symposium of Atomic Energy Research, 1999.
[20] G. Hegyi, A. Keresztúri, I. Trosztel, Z. Elter, ATHLET/KIKO3D results of the OECD/NEA benchmark for coupled codes on KALININ-3 NPP measured data, NENE, Slovenia (September 8–11, 2014).
[21] Benchmark for Uncertainty Analysis in Modelling (UAM) for Design, Operation and Safety Analysis of LWRs, Volume I: Specification and Support Data for the Neutronics Cases (Phase I), NEA/NSC/DOC (2012) 10, 2012.
[22] AER Benchmark Book, Atomic Energy Research (AER), 1999. Budapest.
[23] A. Carreño, A. Vidal-Ferràndiz, D. Ginestar, G. Verdu, Adaptive Time-step Control for Modal Methods to Integrate the Neutron Diffusion Equation.
[24] T. Downar, Y. Xu, V. Seker, N. Hudson, PARCS NRC - v3.3.1 Volume I: Input Manual, June, 2018.
[25] K. Obaidurrahman, J. Doshi, R. Jain, V. Jagannathan, Development and validation of coupled dynamics code 'trikin' for VVER reactors, Nucl. Eng. Technol. 42 (3) (2010) 259–270.
[26] M.B. Chadwick, et al., ENDF/B-VII.0: Next-generation evaluated nuclear data library for nuclear science and technology, Nucl. Data Sheets 107 (12) (2006) 2931–3060, https://doi.org/10.1016/j.nds.2006.11.001.
[27] J.Y. Cho, C.H. Kim, Higher-order polynominal expansion nodal method for hexagonal core neutronics analysis, Ann. Nucl. Energy 25 (13) (1998) 1021–1031.
[28] T. Downar, Y. Xu, V. Seker, PARCS v3.0 U.S. NRC Core Neutronics Simulator Theory Manual, Department of Nuclear Engineering and Radiological Sciences University of Michigan.
[29] H.A. Van Der Vorst, BI-CGSTAB: a fast and smoothly converging variant of BI-CG for the solution of nonsymmetric linear systems, SIAM J. Sci. Stat. Comput. 13 (1992) 631–644.
[30] J. Koyama, M. Aoyaama, Nodal expansion method for solution of diffusion equation in hexagonal geometry, J. Nucl. Sci. Technol. 26 (6) (1989) 636–638, https://doi.org/10.1080/18811248.1989.9734358.
[31] K.B. Park, H.G. Joo, Source expansion nodal method for hexagonal geometry applications, in: Proceedings of the Reactor Physics Asia 2015 (RPHA15) Conference, Jeju, Korea, Sept. 16–18, 2015.
[32] N.Z. Cho, J.M. Noh, Analytic function expansion nodal method for hexagonal geometry, Nucl. Sci. Eng. 121 (1995) 245.
[33] Non-linear Triangle-Based Polynomial Expansion Nodal Method for Hexagonal Core Analysis, KAERI/TR-1652/2000, Korea Atomic Energy Research Institute, 2000.
[34] Benchmark for Neutronic Analysis of Sodium-Cooled Fast Reactor Cores with Various Fuel Types and Core Sizes, Nuclear Science, OECD/NEA, NEA/NSC/R(2015)9, February 2016. https://www.oecd-nea.org/upload/docs/application/pdf/2020-01/nsc-r2015-9.pdf.
[35] V.A. Tereshonok, S.P. Nikonov, M.P. Lizorkin, K. Velkov, A. Pautz, K. Ivanov, Kalinin-3 Coolant Transient Benchmark Switching-Off of One of the Four Operating Main Circulation Pumps at Normal Reactor Power, NEA/NSC/DOC, 2009, p. 5.
[36] G. Hegyi, A. Keresztúri, I. Trosztel, Z. Elter, A THLET/KIKO3D results of the OECD/NEA benchmark for coupled codes on KALININ-3 NPP measured data, in: A. Keresztúri, I. Trosztel, Zs. Elter, Gy, NENE 2014, Slovenia, September 8–11, 2014.
[37] S. Choi, C. Lee, D. Lee, Resonance treatment using pin-based pointwise energy slowing-down method, J. Comput. Phys. 330 (2017) 134–155, https://doi.org/10.1016/j.jcp.2016.11.007.
[38] J. Leppänen, M. Pusa, T. Viitanen, V. Valtavirta, T. Kaltiaisenaho, The Serpent Monte Carlo code: status, development and applications in 2013, Ann. Nucl. Energy 82 (2015) 142–150, https://doi.org/10.1016/j.anucene.2014.08.024.
[39] J. Jang, B. Ebiwonjumi, W. Kim, J. Park, J. Choe, D. Lee, Validation of spent nuclear fuel decay heat calculation by a two-step method, Nucl. Eng. Technol. 53 (1) (2020) 44–60, https://doi.org/10.1016/j.net.2020.06.028.
[40] Studsvik, CASMO5 PWR Methods and Validation Report, SSP-14-P01/012-R Rev. 1, 2015. https://www.nrc.gov/docs/ML1535/ML15355A290.pdf.
[41] N. Soppera, M. Bossant, E. Dupont, JANIS 4: an improved version of the NEA Java-based nuclear data information system, Nucl. Data Sheets 120 (2014) 294–296.
[42] M.B. Chadwick, et al., ENDF/B-VII.1 nuclear data for science and technology: cross sections, covariances, fission product yields and decay data, Nucl. Data Sheets 112 (12) (2011) 2887–2996, https://doi.org/10.1016/j.nds.2011.11.002.
[43] J. Jang, B. Ebiwonjumi, W. Kim, J. Park, D. Lee, Verification and validation of isotope inventory prediction for back-end cycle management by two-step method, Nucl. Eng. Technol. 57 (3) (2021) 2105–2125, https://doi.org/10.1016/j.net.2021.01.009.
[44] T. Bahadir, Improved PWR radial reflector modeling with simulate5, in: Advances in Nuclear Fuel Management V (ANFM 2015), Hilton Head Island, South Carolina, USA, on CD-ROM, American Nuclear Society, LaGrange Park, IL, 2015. March 29–April 1, 2015.
[45] S.A. Ki, Usheva, A.A. Kuten, L.F. Khruschinsky, Babichev, Generation of XS library for the reflector of VVER reactor core using Monte Carlo code Serpent, IOP Conf. Series: Journal of Physics: Conf. Series 781 (2017), 012029, https://doi.org/10.1088/1742-6596/781/1/012029.
[46] P.I.O. Pessoa, L.M. Araujo, F.C. Silva, A.A.M. Menezes, Numerical methods applied to pin power reconstruction based on coarse-mesh nodal calculation, Ann. Nucl. Energy 118 (2018) 291–312, https://doi.org/10.1016/j.anucene.2018.04.010.
[47] S. Choi, C. Lee, D. Lee, Resonance treatment using pin-based pointwise energy slowing-down method, J. Comput. Phys. 330 (2017) 134–155, https://doi.org/10.1016/j.jcp.2016.11.007.
[48] Pre-Operational Inspection Report of Shin-Kori Nuclear Power Plant Unit 3 (Initial Fuel Load and Startup Test, Vol. 2, Korea Institute of Nuclear Safety, 2016. KINS/AR-1008, https://nsic.nssc.go.kr/dta/reguResultView.do?seq=882.
[49] R. Ferrer, J. Hykes, J. Rhodes, Development of CASMO5 for VVER-1000/1200 Analysis and Preliminary Validation Using Critical Experiments, 2019, https://doi.org/10.3139/124.190006.
[50] T. Lötsch, V. Khalimonchuk, A. Kuchin, Proposal of a Benchmark for Core Burnup Calculations for a VVER-1000 Reactor Core, Novel Vision of Scientific & Technical Support for Regulation of Nuclear Energy Safety, 2017. Kyiv, Ukraine, https://inis.iaea.org/collection/NCLCollectionStore/_Public/41/035/41035568.pdf.
[51] VVER-specific Features Regarding Core Degradation, NEA/CSNI/R(98)20, September, 1998. https://www.oecd-nea.org/upload/docs/application/pdf/2020-01/csni-r98-20.pdf.
[52] V. Onufriev, Design and Fabrication of Nuclear Fuel for WWER and RBMK Reactors, Workshop on Modelling and Quality Control for Advanced and Innovative Fuel Technologies, 14-25 November 2005, The Abdu Salam International Centre for Theoretical Physics, Trieste, Italy, https://indico.ictp.it/event/a04215/session/26/contribution/16/material/0/1.pdf.
[53] [Online] The Power Reactor Information System (PRIS), IAEA, https://pris.iaea.org/PRIS/CountryStatistics/ReactorDetails.aspx?current=453.
[54] P. Balestra, C. Parisi, A. Alfonsi, C. Rabiti, Simulation of AER-DYN-002 and AER-DYN-003 Control Rod Ejection Benchmarks by RELAP5-3D/PHISICS Coupled Codes, Nuclear Technology, 193:1, 175-182, https://doi.org/10.13182/NT14-138.
[55] A. Ranta-aho, Validation of depletion codes against VVER-440 spent fuel data, NEA/NSC/DOC(2006), in: 31, the Need for Post Irradiation Experiments to Validate Fuel Depletion Calculation Methodologies Workshop Proceedings, Czech Republic, May 11–12, 2006, https://www.oecd.org/officialdocuments/publicdisplaydocumentpdf/?cote=NEA/NSC/DOC(2006)31&docLanguage=En.